

Amun JARZEMBSKI, Cedric SHASKEY, Keunhan PARK

Review: Tip-based vibrational spectroscopy for nanoscale analysis of emerging energy materials

© Higher Education Press and Springer-Verlag GmbH Germany, part of Springer Nature 2018

Abstract Vibrational spectroscopy is one of the key instrumentations that provide non-invasive investigation of structural and chemical composition for both organic and inorganic materials. However, diffraction of light fundamentally limits the spatial resolution of far-field vibrational spectroscopy to roughly half the wavelength. In this article, we thoroughly review the integration of atomic force microscopy (AFM) with vibrational spectroscopy to enable the nanoscale characterization of emerging energy materials, which has not been possible with far-field optical techniques. The discussed methods utilize the AFM tip as a nanoscopic tool to extract spatially resolved electronic or molecular vibrational resonance spectra of a sample illuminated by a visible or infrared (IR) light source. The absorption of light by electrons or individual functional groups within molecules leads to changes in the sample's thermal response, optical scattering, and atomic force interactions, all of which can be readily probed by an AFM tip. For example, photothermal induced resonance (PTIR) spectroscopy methods measure a sample's local thermal expansion or temperature rise. Therefore, they use the AFM tip as a thermal detector to directly relate absorbed IR light to the thermal response of a sample. Optical scattering methods based on scanning near-field optical microscopy (SNOM) correlate the spectrum of scattered near-field light with molecular vibrational modes. More recently, photo-induced force microscopy (PiFM) has been developed to measure the change of the optical force gradient due to the light absorption by molecular vibrational resonances using AFM's superb sensitivity in detecting tip-sample force interactions. Such recent efforts successfully breach the diffraction limit of light to provide nanoscale spatial resolution of vibrational spectroscopy,

which will become a critical technique for characterizing novel energy materials.

Keywords vibrational spectroscopy, atomic force microscopy, photo-thermal induced resonance, scanning near-field optical microscopy, tip-enhanced Raman spectroscopy, photo-induced force microscopy, molecular resonances, surface phonon polaritons, energy materials

1 Introduction

The power of vibrational spectroscopy stems from the nature of light-matter interactions due to a material's electronic, crystalline, and molecular compositions [1–4]. When a material is illuminated by visible or infrared (IR) light, the incident photons transfer energy to electrons, atomic lattices, and/or molecules in the material, exciting them from their relaxed states to characteristic vibrational modes. The uniqueness of spectral light-matter interactions can be used to recognize materials and identify dominant bonding configurations and electronic and radiative properties, all of which are key to the development of novel energy-related materials. In particular, nanomaterials and nanostructures have unique attributes for the advancement of various energy conversion systems, such as solar cells, thermoelectrics, fuel cells, batteries, and near-field energy conversion which are becoming cornerstone to overcome current challenges in such energy systems [5–7]. With length scales 10^4 times smaller than the width of a typical human hair, nanomaterials and structures possess an exceptionally large surface-to-volume ratio, which is a key parameter in energy transport and conversion phenomena. Moreover, they have several compelling capabilities, such as controlling the direction of energy flow based on their molecular or crystalline structure, manipulating optical fields through plasmonic and phononic resonance excitations, and enhancing photoelectric conversion through near-field optical interactions. Yet, one major challenge in this field is proper non-invasive

Received Jul. 29, 2017; accepted Oct. 22, 2017; online Jan. 18, 2018

Amun JARZEMBSKI, Cedric SHASKEY, Keunhan PARK (✉)
Department of Mechanical Engineering, University of Utah, Salt Lake City, UT 84112, USA
E-mail: kpark@mech.utah.edu

material characterization. Vibrational spectroscopy aims to address this difficulty by utilizing visible through IR light to probe a material's dominant structure, revealing chemical, electronic, thermal, and optical traits.

Vibrational spectroscopy of a material is routinely achieved in the IR region ($\lambda = 2$ to $20\ \mu\text{m}$) by illuminating the sample with either a broadband IR source (i.e., global or synchrotron radiation) or tunable mid-IR laser [4]. The detected IR spectrum provides vibrational resonance peaks at spectral locations corresponding to the photon energy absorbed to excite atomic lattice, electron or molecular vibrations within the material. Alternatively, the Raman effect can also be used to probe the same vibrational phenomena [4]. When incident light, typically in the visible to near-IR region ($\lambda = 0.4$ to $1.5\ \mu\text{m}$) stimulates a material, a small portion of photons are inelastically scattered due to energy interactions between the incident photons and molecular vibrations within the material. Therefore, the spectroscopic measurement of Raman scattering (or Raman spectrum) can identify a material's unique molecular fingerprint. However, the main limitation of conventional vibrational spectroscopy arises from the diffraction limit of light. The spatial resolution of a far-field optical system is fundamentally limited by Abbe's law, i.e., $\Delta x_{\text{min}} = 0.6098\lambda/(\text{NA})$, where NA is the numerical aperture of the optical system and can be as large as 1.4 [8–10]. For example, an IR microscope used to probe carbonyl bonds within polymers typically uses IR radiation around $5\ \mu\text{m}$ yielding an absolute minimum spatial resolution of $2.2\ \mu\text{m}$ at best [2]. Therefore, such a microscope system is unable to resolve localized structures present in heterogeneous materials like grain boundaries, molecular alignment,

material contamination and blending, and material/medium interfaces. By taking vibrational spectroscopy past the Abbe limit, a plethora of research and engineering applications should become accessible.

The present review article covers the integration of atomic force microscopy (AFM) with vibrational spectroscopy (Fig. 1) to realize nanoscale spatially resolved vibrational spectroscopic imaging. The discussion starts with basic background information on the implementation of IR vibrational spectroscopy, Raman scattering, and AFM (Section 2). Sections 3 to 5 present the three main tip-based functional methodologies developed to date to extract vibrational spectra at the nanoscale: photothermal absorption, near-field scattering, and photo-induced force based instrumentations. Each section starts with a description of the fundamental principle including relevant theoretical expressions, then transitions to key experimental realizations that show the capability of the method to reproduce far-field spectra with sub-diffraction limited resolution, and finally presents state-of-the-art research applications where tip-based nanoscale vibrational spectroscopy leads as a novel material characterization technique. Lastly, Section 6 summarizes the capabilities of each technique and provides the future outlooks on the research direction in tip-based vibrational nanospectroscopy.

2 Overview of basic instrumentations

To understand how vibrational spectroscopy works at the nanoscale, conventional far-field vibrational spectroscopies and AFM should be discussed first because these

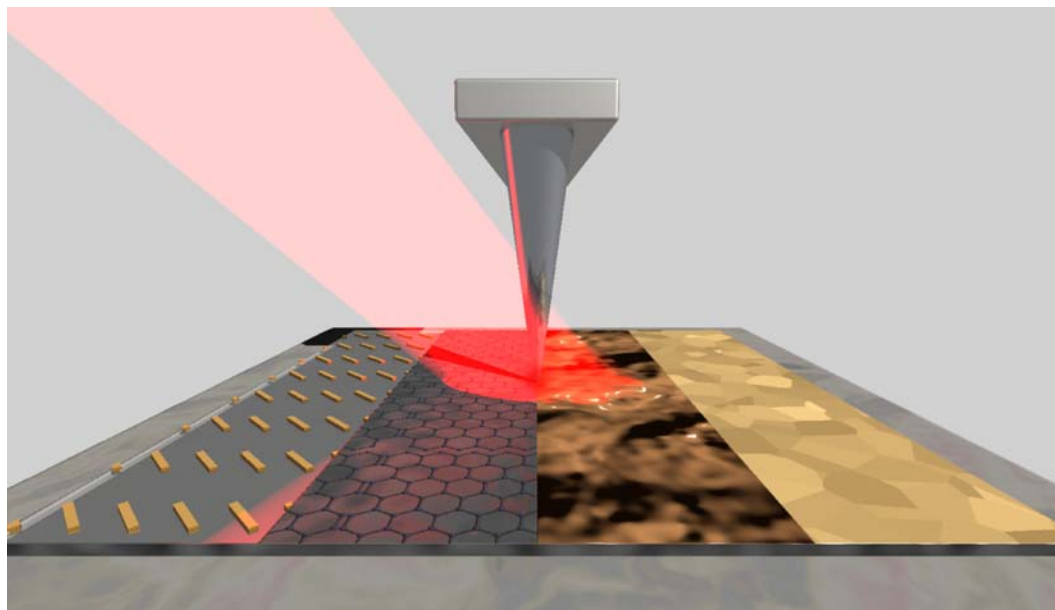


Fig. 1 Tip-based nanoscale vibrational spectroscopy. Atomic force microscopy (AFM) can be integrated with optical-based vibrational spectroscopy to allow nanoscale spectroscopic imaging and analysis for various materials, such as plasmonic nanostructures, 2-D materials, biological samples, and grain boundaries.

instruments act as the building blocks of the nanoscale vibrational techniques to be reviewed. The following section presents the basics of optical absorption using a simple dipole model to illustrate the connection between absorption and a material's optical properties. IR and Raman spectroscopies, which are two main vibrational spectroscopy techniques, will be discussed with a focus on their practical realizations and limitations. The AFM and its pertinent operational configurations will also be presented. The versatility of AFM is highlighted, which ideally suits it as a nanoscale imaging platform for the acquisition of sub-wavelength vibrational spectra.

2.1 Conventional vibrational spectroscopy: IR and Raman

Vibrational spectroscopy essentially measures the absorption of electromagnetic (EM) radiation in a material as a function of wavelength (wavenumber or frequency). When the incoming EM radiation is absorbed by a small particle in a medium, the absorption efficiency can be written as [11]

$$Q_{\text{abs}}(\lambda) \propto \frac{1}{\lambda} \text{Im}[\alpha(\lambda)], \quad (1)$$

which states that optical absorption is proportional to the imaginary part of the particle's electric polarizability, $\alpha(\lambda)$, divided by the wavelength of incident radiation. When the particle is assumed as a point dipole, the electric polarizability is directly related to the wavelength-dependent optical properties as [11]

$$\alpha(\lambda) = 4\pi R^3 \left[\frac{\varepsilon_1 - \varepsilon_m}{\varepsilon_1 - 2\varepsilon_m} \right], \quad (2)$$

where R is the particle radius, and ε_1 and ε_m are the dielectric functions of the material and surrounding media, respectively. If $\varepsilon_1 = -2\varepsilon_m$, resonance conditions are met in Eq. (2) to yield a Lorentzian peak in $Q_{\text{abs}}(\lambda)$ in the spectral domain. Individual materials have unique absorption peaks depending on complex electronic, atomic, and molecular compositions, suggesting that vibrational spectroscopy can provide the chemical and structural fingerprints of a material from the measurement of its absorption (or extinction by including light scattering) spectrum.

The most comprehensive and widely used IR spectroscopy technique is Fourier transform IR (FTIR) spectroscopy, which allows for fast, broadband spectra acquisition [1–3]. Since its first commercial realization in 1969, FTIR has evolved into a powerful tool for the study of a material's chemical bonding [12–16] and for the measurement of a material's optical properties and plasmonic/phononic resonances [17,18]. In FTIR, a broadband illumination source (i.e., global or synchrotron radiation source) is used to provide continuous spectral coverage. A Michelson interferometer develops a temporal interferogram due to the interference of probing and reference

beams at the beam splitter. The interferogram contains time-domain information about the IR absorption of the sample, and by performing a fast Fourier transform (FFT) analysis, the IR spectrum can be obtained over a spectral range determined by the sweeping distance of the reference mirror [2]. Comprehensive descriptions of IR spectroscopy and FTIR can be found elsewhere [1–4].

A vibrational spectrum can also be measured through the inelastic scattering phenomenon known as Raman scattering, named after Sir C.V. Raman who discovered this effect in 1928 [19]. Light-matter interactions induce elastic (Rayleigh) and inelastic (Raman) scattering phenomena. A Raman scattering signal has Stokes and anti-Stokes shifts as a result of energy transfer between the incident photon and the material's molecular vibrational modes. If the initial state of the vibrational mode is not excited, the incident photon will confer energy to the vibrational mode and be re-emitted with less photon energy (or at a longer wavelength), called a Stokes shift. Conversely, if the vibrational mode to which the photon interacts is initially excited, the scattered radiation will experience a blue shift, called anti-Stokes shift by receiving energy from already excited vibrational states [20,21]. Therefore, a Raman spectrum contains vibrational spectroscopic information about the sample and can be used as a molecular identification tool [22]. However, since Rayleigh scattering intensity is much stronger than Raman scattering, the Rayleigh scattering signal should be sufficiently suppressed to acquire the Raman spectrum with a high signal-to-noise ratio. More in depth reviews of Raman spectroscopy can be found elsewhere [4,20,22–25].

The major drawback of conventional vibrational spectroscopy is the diffraction-limited spatial resolution. As briefly discussed in the introduction, Abbe's law fundamentally prevents optical imaging and spectroscopic analysis of a sub-wavelength feature. The best spatial resolution achievable by far-field FTIR is on the order of $\sim 5 \mu\text{m}$ which cannot resolve nanomaterials. A typical spatial resolution of Raman spectroscopy is better than IR spectroscopy due to its use of visible to near-IR light, but it is still challenging to achieve sub-micron spatial resolution. Moreover, Raman spectroscopy has a small Raman scattering cross-section on the order of 10^{-30} cm^2 , often requiring long signal integration time to increase the signal-to-noise ratio to an acceptable level [26].

2.2 Atomic force microscopy

Atomic force microscopy (AFM) was invented in 1986 to realize atomistic-scale imaging past the diffraction limit of light [27–29]. As shown in Fig. 2, the AFM measures the atomic force interactions between a sharp tip, typically integrated at the free end of a microcantilever probe, and a sample surface. While the tip raster-scans over the sample surface, the deflection of the microcantilever is measured typically with a laser reflection scheme to generate a 3-

dimensional topographical image. Many AFMs use a 4-quadrant photo-sensitive detector (PSD) to detect cantilever deflection: see Fig. 2(a). However, in some AFM-based instruments, the interferometric method in Fig. 2(b) may be preferred due to its high sensitivity, compactness, and minimal thermal load [30]. The sensitivity of AFM to detect force is routinely below a few pico-newtons [31,32], leading to superb sub-angstrom topographic resolution in height [33]. While various AFM-based imaging techniques have been developed to date, they are fundamentally based on two basic operational modes — contact and intermittent contact (or tapping) modes. In contact mode, the tip maintains contact with the sample surface and, in most cases, the piezoelectric scanner is feedback-controlled to keep the cantilever deflection (i.e., tip-sample force) constant during scanning [27]. The piezo-scanner traces the sample surface and is used to generate a 3-D topographic image. In intermittent contact mode, the AFM cantilever oscillates at its resonant frequency, such that the cantilever tip gently taps on the sample surface [28]. The cantilever oscillation amplitude is maintained constant during scanning by feedback-controlling the piezo-scanner, such that the piezo-stage traces the sample topography. When compared to contact mode, intermittent-contact mode barely touches a sample surface with a minimal shear force, which is ideally suited for the imaging of soft samples and minimizes the wear and/or contamination of the tip. Better image quality is another expected advantage of intermittent-contact mode due to its use of lock-in detection. Thorough reviews on AFM and its

applications are available and can be found in Refs. [31,33–38].

Recently, significant efforts have been made to implement vibrational spectroscopic techniques for the structural, physical, and chemical analysis of nanomaterials and structures by overcoming its diffraction limit. As one potential approach, AFM has been integrated with vibrational spectroscopy to make use of AFM's nanoscale imaging capability and superb sensitivity in force detection. In the following sections, we will review the previous advancements of tip-based vibrational nanospectroscopy in the AFM platform.

3 Photothermal induced resonance nanospectroscopy

It is well known that absorbed photon energy due to molecular vibrational resonances is dissipated as heat, resulting in temperature rise and thermal expansion of the light-illuminated area. Photothermal induced resonance (PTIR) nanospectroscopy correlates this photothermal energy conversion to the vibrational spectrum of a sample by utilizing the AFM tip as a nanoscopic tool to measure either the local temperature rise [39–44] or thermal expansion [44–67]. The measurement of local temperature rise requires the use of a thermal profiler probe such as a passive thermocouple probe [68–71], Wollaston wire probe [39–41], or resistive thermometer probe [43,72,73] in a scanning thermal microscopy (SThM) platform [42].

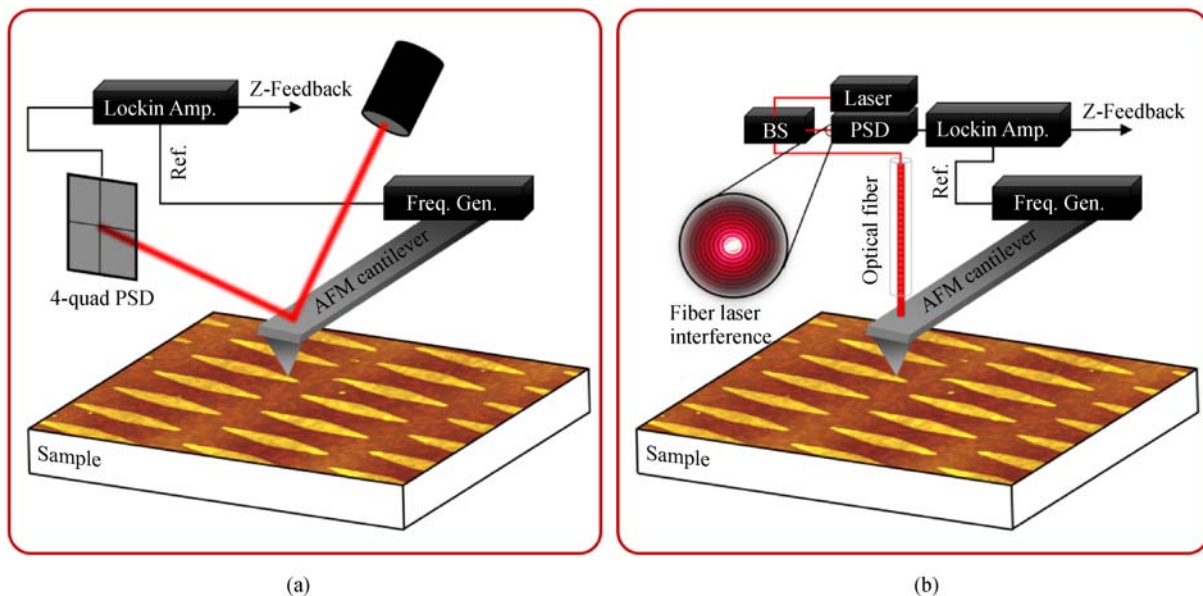


Fig. 2 Atomic force microscopy (AFM). (a) Schematic of an AFM that detects cantilever deflection/oscillation using a 4-quadrant photosensitive detector (PSD). (b) Schematic of an interferometric AFM that creates a Fabry-Perot cavity between the optical fiber/air interface and AFM cantilever. A beamsplitter (BS) is used to send the interference pattern to a PSD [30].

The Wollaston wire probe is by far the simplest thermal profiler consisting of a thin, bent platinum wire. However, its probe-sample contact area is several hundred nanometers at smallest [39]. While micro-machined thermocouple and resistive probes can achieve a sub-100 nm spatial resolution [44,70,71], their temperature resolutions are on the order of 100 mK in DC mode, which can be improved to 1 mK in AC mode after implementing lock-in detection [42,71,74]. Such temperature resolutions are not good enough to measure the local temperature rise due to vibrational photothermal absorption with high signal-to-noise ratio. Moreover, thermal probes are prohibitively expensive to design and fabricate, and often require a special probe holder for electrical packaging [44]. Compared to the local temperature measurement, the measurement of local thermal expansion is relatively easy and does not need a functionalized AFM probe [58]. By taking advantage of the AFM's sub-nanometer resolution in topographical mapping, thermal expansion PTIR has achieved nanospectroscopic imaging of various samples, such as living cells [48], viruses and bacteria [46,47], polymers [51–54], and plasmonic resonators [63–65]. Therefore, this review will only focus on thermal expansion PTIR and its use for the nanoscale analysis of energy-related materials.

3.1 Basic principles of thermal expansion PTIR

In a typical PTIR setup, an AFM probe is in contact with a sample that is deposited directly onto a prism. A tunable mid-IR laser provides backside-illumination at an incidence angle bigger than the critical angle to achieve total

internal reflection (TIR): see Fig. 3(a) [45]. As shown in Fig. 3(b), TIR generates an exponentially decaying evanescent electromagnetic (EM) field at the prism/sample interface, which interacts with the sample while minimizing residual absorption by the tip. When the laser is tuned to an absorption band of the sample, light absorption owing to the interactions between the evanescent field and the sample causes local heating and, consequently, thermal expansion. Particularly, when a short pulsed laser is pumped to the sample, photothermal expansion is strong enough to excite the contact resonance of the cantilever placed on the laser-illuminated spot. As a result, the cantilever sharply oscillates with a high amplitude and ring-down decays on the order of $\sim 100 \mu\text{s}$. FFT analysis of the ring-down decay pattern in the frequency domain reveals the presence of multiple resonance modes of the cantilever due to nonlinear cantilever dynamics under contact resonance [55]. The sample's absorption spectrum is generated by plotting the maximum values of the ring-down oscillation of the cantilever for different illumination wavelengths, where larger cantilever oscillations correspond to stronger optical absorption. In addition, the cantilever modal response provides unique information about the thermal dependence of the sample's stiffness [58].

Light-matter interactions in the PTIR technique is fundamentally understood as a conduction heat transfer problem with laser absorption as the applied heat source. Dazzi et al. [75] conducted the thermomechanical analysis of thermal expansion PTIR on a spherical particle sample in a thin-film template (typically $\lambda \leq 2 \mu\text{m}$ in thickness). Figure 3(b) illustrates the schematic of this thermal

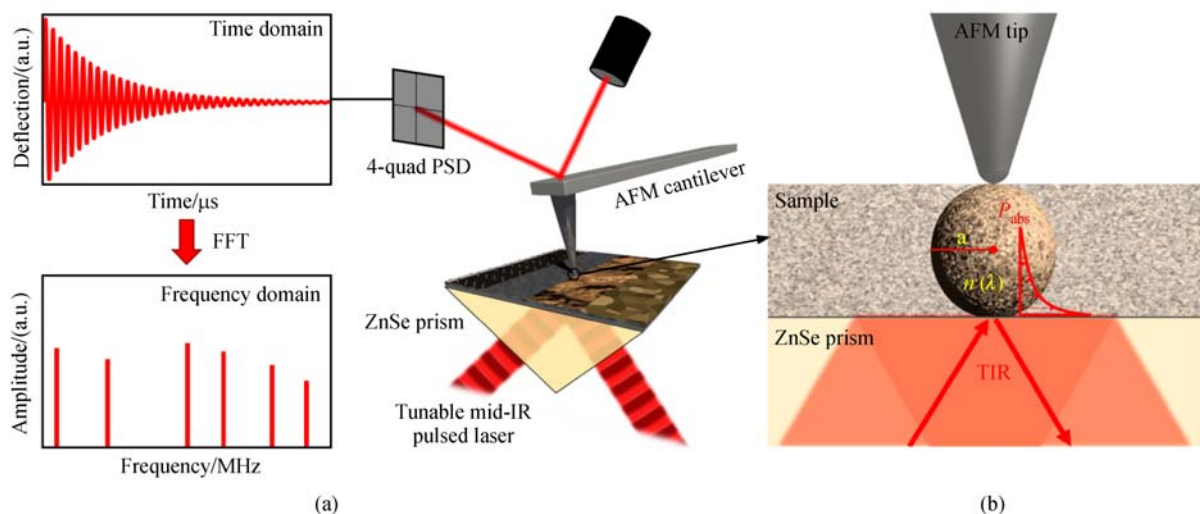


Fig. 3 Photo-thermal induced resonance (PTIR). (a) Typical PTIR setup, where the sample is deposited on a zinc-selenide (ZnSe) prism [45]. A tunable pulsed laser (t_p of 10^{-9} s) reflects off of the prism-sample interface through total-internal reflection. A standard AFM tip is in direct contact with the sample, generating the temporal ring-down oscillation upon the absorption of the pulsed laser. The FFT analysis of the ring-down cantilever oscillation provides the modal response of the AFM cantilever. (b) Close-up of the tip-sample-prism interfaces. The sample is modeled as a sphere that has a sub-wavelength radius ($a < \lambda$) and the complex refractive index $\tilde{n}(\lambda)$ [75].

expansion PTIR model, where the spherical particle radius is assumed to be smaller than the laser wavelength (i.e., $a < \lambda$) and have small absorption corresponding to weak molecular vibrations (i.e., $\text{Re}[\tilde{n}^2] \ll \text{Im}[\tilde{n}^2]$). Under these conditions, we can assume that the electric field is uniform across the sample. Thus, the sample can be considered as an electric dipole, and the laser power density absorbed by the sample can be approximated by the following equation [75]:

$$P_{\text{abs}} = \frac{18\pi c \epsilon_0}{\lambda} \frac{\text{Im}[\tilde{n}] \text{Re}[\tilde{n}]}{[\text{Re}[(\tilde{n})^2 + 2]]^2} |E|^2, \quad (3)$$

where \tilde{n} is the complex refractive index of the particle and $|E|^2$ is the intensity of the incident light. Using the heat diffusion equation, the sphere's instantaneous temperature, T_s , can be derived from the absorbed laser power:

$$\rho_s c_s \frac{\partial T_s}{\partial t} = P_{\text{abs}} \Pi(t_p) + k_s \nabla^2 T_s, \quad (4)$$

where ρ_s , c_s , and k_s are the density, specific heat, and thermal conductivity of the spherical particle, respectively, t_p is the laser pulse width, and $\Pi(t_p)$ is a unit temporal block function of length t_p (i.e., $\Pi = 1$ for $t \leq t_p$ and $\Pi = 0$ for $t > t_p$). The duration time of the laser pulse is a critical factor that determines the sensitivity of thermal expansion PTIR, and is typically much smaller than the thermal diffusion time constant, i.e., $\tau_d = a^2/3\alpha_s$, where α_s is the thermal diffusivity of the sphere sample. The typical pulse duration is on the order of a nanosecond. For such short laser pulse, the transient sample temperature can be solved from Eq. (4) to yield [75]

$$T_s(t) = \begin{cases} \frac{T_{\text{max}}}{t_p} t, & 0 \leq t \leq t_p, \\ T_{\text{max}} \exp\left[-\frac{t_p - t}{\tau_d}\right], & t_p \leq t \end{cases} \quad (5)$$

indicating that the particle temperature linearly increases up to $T_{\text{max}} = P_{\text{abs}} t_p / \rho_s c_s$ during the laser pulse and exponentially decays afterwards [58]. The corresponding relative thermal expansion of the particle, defined as the change of the particle's radius normalized by the original radius, is given by [75]

$$\left[\frac{da(t)}{a} \right] = \frac{1}{3} \beta_{\text{exp}} T_s(t), \quad (6)$$

which shows that the relative thermal expansion is proportional to the sphere temperature through the material-dependent thermal expansion coefficient, β_{exp} [58,75]. The thermal expansion therefore follows the transient temperature profile described by Eq. (5). Using the above expressions, a typical temperature rise in a thin-film polymer sample is below 10 K, which is equivalent to tens of picometers of thermal expansion [75]. This small thermal expansion would be challenging to measure with a

static AFM operation, suggesting that the mechanical resonance of a cantilever probe should be implemented to amplify the thermal expansion signal upon the pulsed laser excitation. Given the tip in contact with the sample, the cantilever modal response is governed by the sample thermal expansion, and in a similar fashion, exhibits exponentially decaying oscillations after laser excitation.

PTIR's spatial resolution is not a strong function of illumination wavelength, and is primarily governed by the tip sharpness, sample thermal properties and thickness [52]. However, by shortening the laser pulse, heat diffusion effects can be minimized, and for thin samples, the spatial resolution ultimately becomes only a function of tip sharpness. Most often a tunable, nanosecond-pulsed IR laser sources, e.g., CO₂ [75], optical parametric oscillator (OPO) [65], quantum cascade laser (QCL) [76], and a free-electron picosecond laser [48] are used as a light source for PTIR. Recently, PTIR has been configured with a synchrotron radiation source to achieve broadband spectra [44]. Photothermal expansion of self-assembled monolayers (SAMs) was also measured by implementing scanning tunneling microscopy (STM) for PTIR [76].

3.2 PTIR vibrational spectroscopy

As discussed in the previous section, the strength of the signal in thermal expansion PTIR is heavily dependent on the sample's thermal properties. Since materials that have a low thermal capacity and large thermal expansion are ideally suited for the PTIR measurement scheme, polymeric materials have been intensively used as a sample material for PTIR. Polymers have received keen attention for energy applications, such as fuel cells, batteries, and thin-film solar cells, which often requires nanoscale molecular and chemical information to further improve energy performance [77–79]. Furthermore, polymers provide a good benchmark to ensure consistency between nanoscale vibrational spectra and conventional spectral databases, allowing unambiguous data interpretation and nanoscale material characterization. Figure 4(a) and (b) show the AFM topography and PTIR spectra collected on a Poly(methyl methacrylate) (PMMA) microdisk (10 μm in diameter) surrounded by an epoxy resin [54]. As shown in Fig. 4(b), PTIR clearly distinguishes the IR spectra of the PMMA microdisk and the surrounding epoxy resin. The PTIR spectrum of the PMMA microdisk exhibits the expected C = O molecular resonance at 1730 cm^{-1} as well as other molecular vibrations between 1400–1500 cm^{-1} and 1200–1300 cm^{-1} , while that of the epoxy resin does not show the C = O resonance. Besides its thermophysical properties, the thickness of a sample may have a significant effect to the sensitivity of PTIR spectroscopy. Figure 4(c) and (d) show the dependence of the PTIR spectrum and its signal intensity at C = O on the thickness of PMMA film [54]. The presence of the optimal sample thickness is attributed to the nature of the evanescent EM field

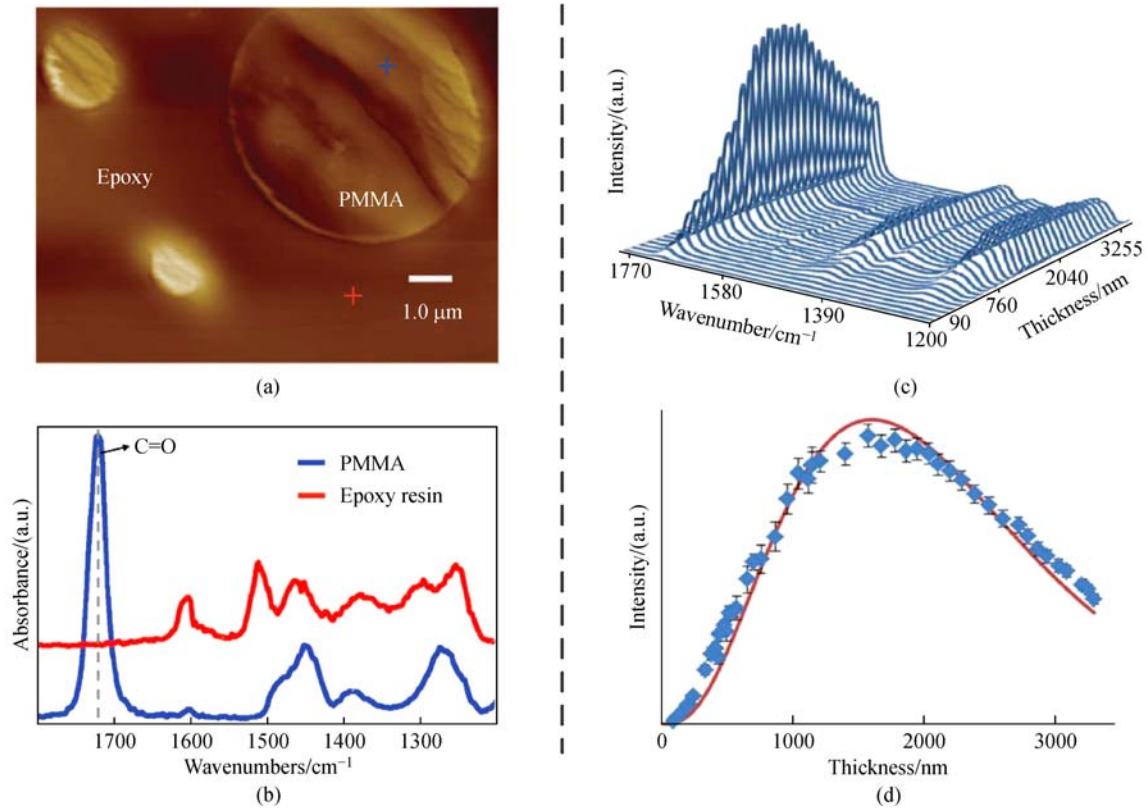


Fig. 4 PTIR measurement of weak molecular resonances in PMMA [54]. (a) Topography of a PMMA microdisk embedded in an epoxy resin. (b) PTIR spectra for the PMMA microdisk and the epoxy resin taken at the locations identified by the crosses in (a). The PTIR spectra shows the C=O vibrational resonance of PMMA at 1730 cm⁻¹. (c) The dependence of the PTIR signal on the PMMA layer thickness. (d) The maximum intensity of the C=O vibration as a function of PMMA thickness demonstrates a strong dependence of the PTIR signal on sample thickness. The solid curve represents the theoretical model. Adapted with permission from Ref. [54]. Copyrighted by Wiley-VCH.

penetrating through a sample under the TIR condition. When the TIR illumination scheme is taken into account, the exponentially decaying evanescent field within the sample can be expressed as $E(z) = E_0 \exp(-z/d_p)$, where E_0 is the incident electric field and d_p is the penetration depth of the evanescent field into the sample. For a thin-film sample with a thickness, d , the photothermal expansion of the sample should be proportional to $d^3 \exp(-2d/d_p)$, where d^3 represents the sample volume under consideration and $\exp(-2d/d_p)$ represents a temperature rise upon the absorption of the evanescent field. Albeit simple, this model is in good agreement with the measurement shown in Fig. 4(d), suggesting that the sample thickness should be carefully determined to maximize the PTIR signal. According to Fig. 4(d), the optimal film thickness for PTIR is around 1 μm ($d_{\max} \approx 1.8 \mu\text{m}$). However, thin-film samples of ~100 nm in thickness are routinely measured by PTIR [61,64], and a polymer film thinner than 10 nm could generate sufficient PTIR signals [53].

In addition to polymeric samples, metallic nanostructures or metamaterials have been of primary interest to the nanoscale spectroscopy community as they can effectively manipulate light-matter interactions through plasmonic or

phononic resonances. However, metallic structures typically have high thermal conductivity and low thermal expansion coefficients, which makes it challenging to use the PTIR technique for the nanospectroscopic studies of plasmonic behaviors [65]. Lahiri et al. [64] made the first PTIR analysis of localized surface plasmon resonances using a gold asymmetric split ring resonator (ASRR) array coated by a 200 nm PMMA layer. The PMMA acts as a mechanical amplifier to enhance the PTIR response due to light absorption by the ASRR. While a clever idea, the obtained PTIR signal did not yield high spatial resolution due to large parasitic absorption by the PMMA overlayer. Further efforts were made to obtain the PTIR spectroscopic image of plasmonic resonance without the use of a polymer overlayer. Figure 5(a)–(d) shows PTIR images of a bare ASRR without a polymer overlayer [65]. The three images (b)–(d) are PTIR images taken at three different wavenumbers marked as dashed lines in Fig. 5(a), showing that the asymmetric geometry excites plasmonic resonances at different wavenumbers (i.e., the short side resonates around 1432 cm⁻¹ and the longer side at 1268 cm⁻¹). However, metallic structures are still challenging for PTIR measurement, often requiring a tedious,

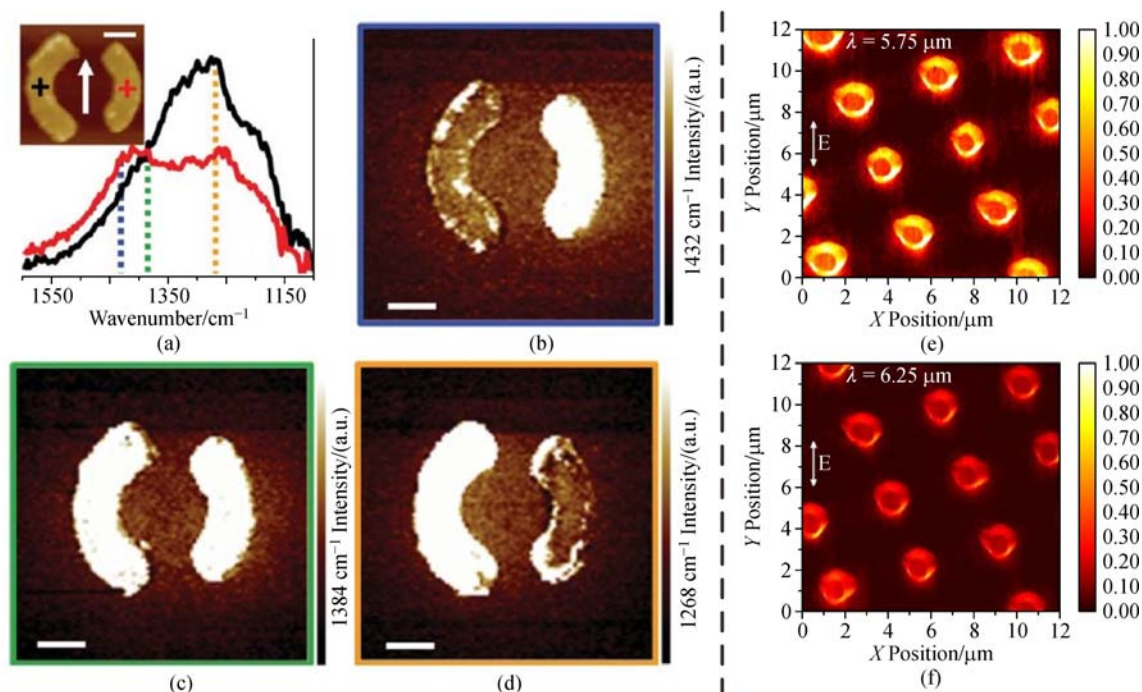


Fig. 5 Localized surface plasmon resonances probed with PTIR [63,65]. (a) The AFM topography of a gold asymmetric split ring resonator (ASRR) (inset) and PTIR spectra taken at the locations indicated by cross marks [65]. Black and red spectra correspond to the larger and smaller resonators, respectively. (b–d) PTIR spectral images of the ASRR at (b) 1432 cm^{-1} (blue dashed line in (a)), (c) 1384 cm^{-1} (green line), and (d) 1268 cm^{-1} (yellow line). (e,f) PTIR spectral images of an indium arsenide (InAs) micropillar array at two wavelengths: 5.75 μm and 6.25 μm , respectively, clearly showing the excitation of localized surface plasmons at 5.75 μm [63]. (a–d) and (e,f) adapted with permission from Refs. [65] and [63], respectively. Copyrighted by (a–d) Wiley-VCH and (e,f) AIP Publishing.

iterative laser alignment procedure to optimize the signal [65]. Heavily-doped semiconductors are better suited to probe plasmonic resonances using PTIR due to their increased photothermal responses [63]. Figure 5(e) and (f) compare PTIR images of a heavily-doped indium arsenide (InAs) micropillar array when the localized surface plasmon is excited at $\lambda = 5.75 \mu\text{m}$ and not excited at $\lambda = 6.25 \mu\text{m}$ clearly demonstrating that the electric field is highly concentrated at the edge of the micropillar upon the excitation of the plasmonic resonance. These results demonstrate that plasmonic structures can be characterized with the PTIR technique, but its routine implementation is far from applicable for the variety of plasmonic/phononic resonators.

Another exciting application of vibrational nanospectroscopy is material characterization at the monolayer level, which will ultimately enable single molecule analysis. Vibrational spectroscopy of monolayers requires precision instrumentation sensitive to small light absorption [80], and for thermal expansion based PTIR, requires picometer-level detection of sample expansion from highly confined areas [62,76]. Figure 6 shows PTIR vibrational spectroscopy performed on self-assembled monolayers (SAMs) using (a) traditional AFM-based PTIR [62] and (b) a novel STM-based PTIR scheme [76]. The AFM-based PTIR spectrum in Fig. 6(a) was obtained on a SAM of 4-

nitrothiophenol (NTP) deposited on an Au substrate [62]. The PTIR spectrum (blue circles) is in good agreement with the reference data (red curve), measured with surface enhanced infrared spectroscopy, which exhibits the symmetric NO_2 stretching resonance at 1339 cm^{-1} . The NTP monolayer is estimated to have a thickness well below 1 nm, which may yield a photothermal temperature rise less than 6 K and the consequent static thermal expansion of approximately 3 pm. This is an estimation based on the experimental conditions where a 160-ns pulsed QCL (laser peak power of 500 mW) is tuned to the resonance at 1339 cm^{-1} . To achieve PTIR sensitivity at this level, the laser pulse repetition rate was set to match the contact resonance frequency between the AFM probe tip and the sample surface, such that the laser pulses could excite the contact resonance of the cantilever through photothermal expansion. The contact resonance of the cantilever could amplify the SAM's thermal expansion signal from ~ 3 pm to ~ 100 pm [62]. Moreover, the AFM tip was coated with gold to concentrate the electric field underneath the tip due to the optical antenna effect between the Au-coated tip and the Au substrate [8]. These two enhancement mechanisms (e.g., contact resonance and antenna effect) can potentially amplify the PTIR signal by up to 10^7 fold, opening the feasibility to perform PTIR on atomically thin samples.

A different monolayer-level PTIR scheme has been

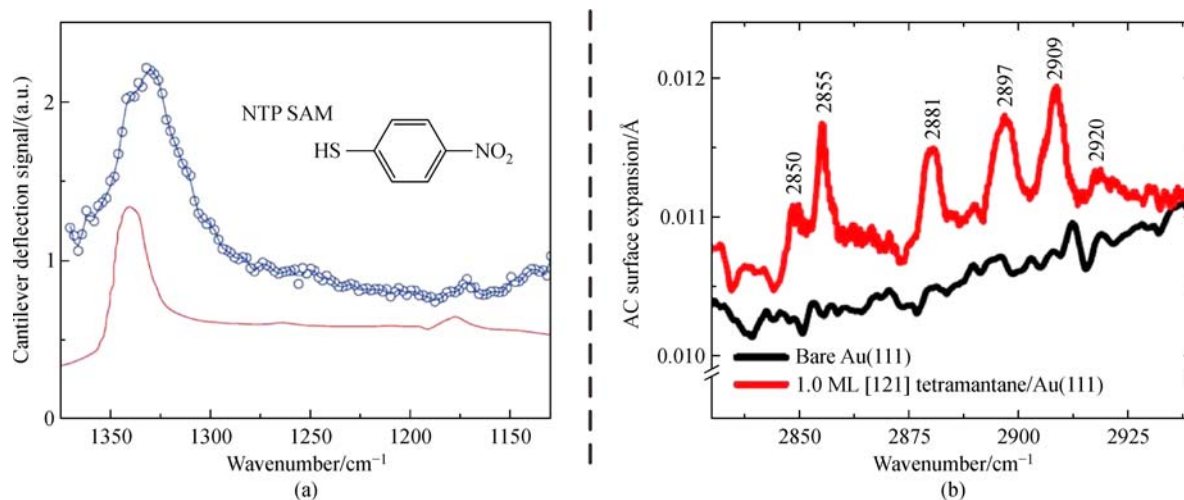


Fig. 6 Monolayer vibrational spectroscopy performed with AFM- [62] and STM-based PTIR [76]. (a) AFM-based PTIR spectra (blue circles) of a 4-nitrothiophenol (NTP) self-assembled monolayer (SAM) on an Au substrate [62]. PTIR spectra is compared with the expected IR spectra (red curve) from Ref. [80]. (b) STM-based PTIR spectra taken on a monolayer of tetramantane (red) and bare Au (black) showing sub-picometer z -expansion resolution [76]. (a) and (b) adapted with permission from Refs. [62] and [76], respectively. Copyrighted by (a) Nature Publishing Group and (b) the American Physical Society.

developed based on the high sensitivity of scanning tunneling microscopy (STM) [76]. The STM-based PTIR method measures a sample's absorption spectrum by detecting thermal expansion through changes in tunneling current. Here a SAM of the sample is deposited on a conducting substrate such that current is allowed to tunnel from the STM tip through the monolayer to the substrate, where the tunneling current is highly sensitive to changes in monolayer thickness. Furthermore, since the current must tunnel through the sample, monolayers are best suited for this type of measurement to minimally impede STM operation. Figure 6(b) shows a vibrational spectra of a self-assembled tetramantane monolayer deposited on an Au substrate [76]. When compared to IR spectrum of a bare Au substrate, vibrational modes of tetramantane are clearly visible in the obtained PTIR spectrum although the chemical fingerprint associated with each mode is not fully identified. The sensitivity analysis of the obtained PTIR signal confirmed that the STM-based method could yield a sub-picometer resolution in the z -direction when the incident IR laser was modulated at 13 Hz. This superb sensitivity is owing to the imaging capability of STM at the atomic level in ultrahigh vacuum and cryogenic conditions. However, this high-end system requirement prevents a routine use of STM-based PTIR techniques.

4 Tip-enhanced near-field nanospectroscopy

Tip-enhanced near-field vibrational spectroscopy is based on scanning near-field optical microscopy (SNOM), which enables optical imaging past the diffraction limit by

confining light to a nano-aperture (i.e., aperture-type SNOM) [81–89] or to a sharp metallic tip (i.e., scattering-type SNOM) [90–95]. Aperture-type SNOM guides light through a sub-100 nm aperture at the end of a metal-coated scanning probe to confine light on the order of the aperture diameter. The confined light is then scattered off the sample and collected with a microscope objective lens for imaging. Since the collected light is solely due to light transmitting through the aperture, aperture-type SNOM can generate a subwavelength optical image whose spatial resolution is governed by the aperture diameter. Spatial resolutions up to $\lambda/20$ have been reported for aperture-type SNOM [83]. However, the diameter of the nano-aperture cannot be smaller than twice the material skin depth (i.e., ~ 10 nm) [8], and the transmissive nature of aperture-type SNOM limits the wavelength versatility of the technique. To surpass the inherent limits of aperture-type SNOM, scattering-type SNOM (s-SNOM) uses a metalized AFM tip as a near-field antenna to scatter light confined at its apex [90–145]. The tip-scattered light contains the local optical properties of the sample directly below the tip, suggesting that the spatial resolution of s-SNOM should be only dependent on the tip sharpness. s-SNOM has been implemented with visible light [96–102]; however, its application to the IR and THz spectra has received more attention where spatial resolutions far less than the diffraction limit have been reported [103–110]. For example, Huber et al. [110] achieved a spatial resolution of $\lambda/3000$ (i.e., ~ 40 nm) by focusing 2.54-THz radiation onto a Pt-coated AFM probe tip. The applicability of tip-scattering measurements to such a broad spectral range, visible to THz, presents a compelling advantage of using s-SNOM for broadband nanospectroscopy. In the subsequent

sections, we will discuss the underlying physics of s-SNOM, followed by thorough review of two s-SNOM based vibrational spectroscopies, i.e., tip-enhanced IR spectroscopy and tip-enhanced Raman spectroscopy.

4.1 Basic principles of s-SNOM

In s-SNOM, the incident light is focused to the apex of a metal-coated AFM tip using an objective lens or focusing mirror as shown in Fig. 7(a). The AFM tip interacts with the incident radiation to create an evanescent EM field above the sample surface [8]. With the tip in close proximity to the sample, the evanescent near-field scatters into the far-field containing information about the sample spatially confined to the tip. The experimental difficulty in s-SNOM is the elimination of the background signal (E_B) originating from reflection off of the sample, tip shaft, and cantilever [106–108]. E_B is not associated with the near-field signal (E_N) and can lead to optical contrast artifacts that void the usefulness of near-field measurements. In general, the detected electric field, E_D , can be expressed as $E_D = E_N + E_B$; therefore, the detected intensity, u_D , is proportional to $|E_D|^2$ to yield [106–108]

$$\mu_D \propto |E_N|^2 + |E_B|^2 + 2E_N E_B, \quad (7)$$

where two distinct background contributions exist: the additive component ($|E_B|^2$) and the multiplicative component ($2E_N E_B$). By operating the AFM tip in intermittent contact mode with oscillation frequency Ω , the nonlinear tip-sample mechanical and near-field optical interactions generate higher harmonic components in the tip-scattered optical signal [104,106]. Therefore, E_N should have high-order frequency components at 2Ω , 3Ω and more, while E_B will only have 0Ω and 1Ω components. By demodulating u_D at higher harmonic frequencies, $|E_B|^2$ can be removed from Eq. (7); however, the multiplicative component still exists and should be suppressed to acquire pure near-field information from the tip-scattered optical signal [106].

To suppress the multiplicative background component ($2E_N E_B$), several interferometric detection techniques, such as homodyne [121], heterodyne [96], pseudoheterodyne [106], and holography [108], have been adopted to s-SNOM, where they are compared in Refs. [106–108]. The key component in the interferometric detection of tip-scattered light is the asymmetric Michelson interferometer as illustrated in Fig. 7(a). By positioning or moving a piezo-actuated reference mirror, a stable reference beam with a controllable phase interferes with the tip-scattered beam at the beam splitter. The detected intensity coupled with the reference beam is expressed as

$$\begin{aligned} \mu_D \propto & |E_N|^2 + |E_B|^2 + |E_R|^2 + 2E_N E_B + 2E_N E_R \\ & + 2E_B E_R, \end{aligned} \quad (8)$$

where E_R is the electric field associated with the reference beam. In the homodyne scheme, higher harmonic demodulation of the tip-scattered optical signal only leaves the components with E_N . In general, $|E_N|^2$ is much smaller than the interference components, and if $E_R \gg E_B$, the interference between the near-field signal and reference beam (i.e., $E_N E_R$) effectively suppresses the uncontrolled background interference (i.e., $E_B E_R$) [106–108]. However, in situations where $E_R \sim E_B$, the homodyne scheme may not be sufficient enough to suppress background artifacts. For complete background suppression, Ocelic et al. [106] suggested pseudoheterodyne interferometry, which oscillates the reference mirror at a frequency M much lower than Ω . The phase-modulated reference beam interferes with the tip-scattered light and the resulting optical signal develops sidebands around the harmonics of Ω . Extraction of the signal at the sidebands of the higher harmonics (e.g., $2\Omega + 1M$) completely suppresses both multiplicative ($2E_N E_B$) and additive ($|E_B|^2$) background contributions. Both techniques have the capability of extracting a sample's absorption spectrum from tip-scattering by separating the near-field amplitude and phase components [106–108]. However, the homodyne scheme has a significantly better signal-to-noise ratio because it does not require sideband detection. Detailed discussions on background elimination in s-SNOM can be found elsewhere [106–109].

s-SNOM measurements do not solely give the optical information of the sample because tip-scattered light is inherently a result of tip-sample near-field interactions. Therefore, the effect of the tip on the detected signal must be understood before the experimental extraction of the sample's optical properties [107]. The scattering coefficient of the tip-sample optical system for p -polarized incident light can be written as [107,127]

$$\sigma = \frac{E_d}{E_i} = f_\sigma (1 + r_p)^2 \alpha_{\text{eff}}, \quad (9)$$

where f_σ represents experimental parameters (e.g., detection location, etc.), r_p is the Fresnel reflection coefficient of the sample, and α_{eff} is the z -component of the tip's effective polarizability including interactions with the sample. It should be noted that the effective polarizability is essentially a tensor due to interactions of the electric field and dipole moment in three directions. However, due to the elongated geometry of the tip, the z -component of the effective polarizability is dominant and is only considered for simple modeling. The simplest model for α_{eff} is the point dipole model (PDM) that considers the tip as a spherical point dipole located at the tip apex position: see Fig. 7(b). Due to its simplicity, the PDM has been widely used to interpret tip-based optical measurements [101–105]. The PDM-based effective polarizability can be derived by considering recursive interactions between the tip dipole and its image dipole in the substrate under the

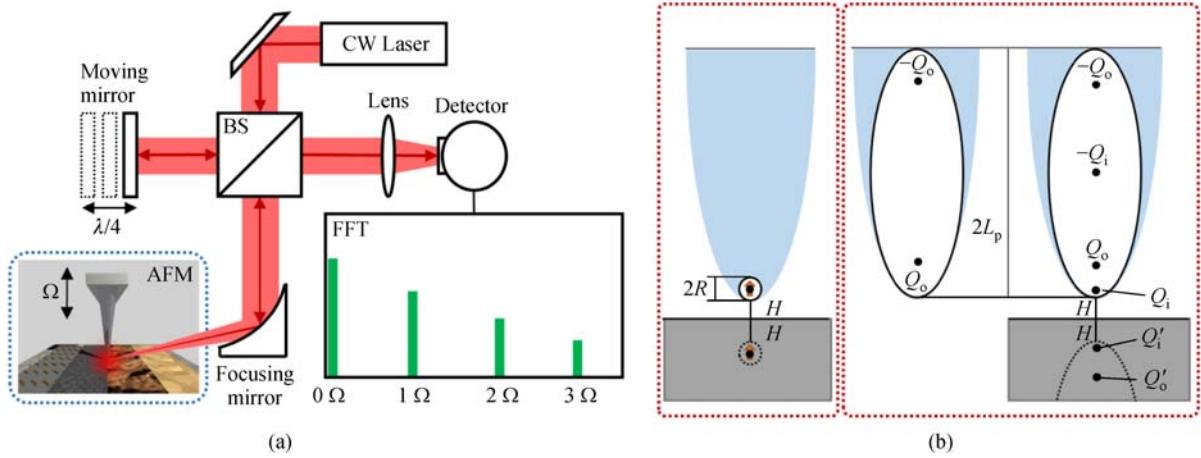


Fig. 7 Schematics of scattering-type Scanning Near-field Optical Microscopy (s-SNOM). (a) s-SNOM using a continuous wave (CW) laser and homodyne interferometric detection of the tip-scattered signal. The moving mirror is shifted between two locations separated by $\lambda/4$ to extract both amplitude and phase information [108]. Tip-substrate near-field interactions can be modeled with either (b) the point dipole model (PDM) or (c) finite dipole model (FDM) [107,148]. (b) and (c) adapted with permission from Ref. [148]. Copyrighted by Elsevier.

quasi-static approximation [147,148]:

$$\overset{\leftrightarrow}{\alpha}_{\text{eff}} = \frac{\alpha_0}{1 - \overset{\leftrightarrow}{G}_R(r_t, r_t)}, \quad (10)$$

where α_0 is the bare polarizability of the tip dipole expressed by the well-known Clausius-Mossotti relation, $\overset{\leftrightarrow}{\alpha}_{\text{eff}}$, i.e., Eq. (2), and $\overset{\leftrightarrow}{G}_R(r_t, r_t)$ is the dyadic reflection Green's function evaluated at the tip position, r_t , which contains the sample's optical properties [8,147,148]. The PDM has given insight about the acquired near-field signals in s-SNOM based spectroscopy including the qualitative spectral locations of vibrational peaks and the expected optical contrast between materials [101–105]. However, the PDM is valid only when the tip-substrate gap distance is much greater than the tip radius [147,148], which limits its applicability in the quantitative analysis of s-SNOM spectra. Additionally, a considerable spectral shift for the surface phonon polariton resonance peak, often up to 60 cm^{-1} , has been reported when s-SNOM was used to acquire the nanoscale mid-IR spectra of polar materials, such as SiC and SiO₂ [111–113]. This spectral red shift could not be explained with the PDM, and necessitates more advanced models [149].

To address the inherent limitations of the PDM, several tip-substrate near-field interaction models have been suggested. Among them, the finite dipole model (FDM) may be perhaps the simplest one that reflects the complicated charge distribution in the tip's elongated geometry when the tip-substrate gap distance is below the PDM limit [107,149]. There are numerical techniques for modeling the tip-substrate near-field interaction in s-SNOM such as the lightning rod model based on a quasistatic boundary element method [134], boundary

element method [150], multiple-multipole method [151], finite element method [152–154], multipole expansion [155], and finite-difference time-domain [156]. Although these more numerically intensive methods may offer better accuracy in the calculation of tip-substrate near-field interactions, they are prohibitively slow in spectral calculations and the comparison with s-SNOM data for the extraction of the sample's optical properties. Figure 7 (c) illustrates the schematics of the FDM with and without the presence of the sample. When the tip is not engaged to the sample surface, the tip is modeled as a prolate spheroid that has monopoles (or point charges) Q_0 and $-Q_0$ under external light illumination. When the tip enters the near-field regime, the bottom monopole of the tip, Q_0 , interacts with the sample to form the mirror image Q'_0 , which acts back on the tip to induce Q_i . These near-field interactions between point charges are recursive [107,149]. In addition, $-Q_i$ should be formed in the tip to satisfy the charge neutrality condition on the tip surface. Such point charge distribution along the major axis of the prolate spheroid creates an effective polarizability tensor, whose z -component can be derived as [107,148,149]

$$\alpha_{\text{eff}} = 2w^2 L_p^3 (\gamma_0 - 1) (\eta + 1), \quad (11)$$

where L_p is the length of the semi-major axis, w is the location of Q_0 from either spheroid apex normalized by L_p , r_0 is the electric field enhancement at the spheroid apex due to external illumination, and η is the complex function that contains information about the tip-substrate recursive interactions: more details can be found in Refs. [107,148,149]. It should be noted that $2w^2 L_p^3 (\gamma_0 - 1)$ in the above equation represents the z -component of the bare polarizability for the spheroid [148]. Therefore, the

effective polarizability can be greatly enhanced due to tip-substrate near-field interactions, as indicated by $(\eta + 1)$. The FDM has shown good correlations with experimental results [107,127,132,149], suggesting that the dielectric function of a material can be extracted by comparing the measured scattering coefficient with Eq. (9) coupled with Eq. (11). However, since f_{σ} and r_p are unknown, the scattering coefficient, σ , should be normalized by that of a known reference sample (e.g., Au or Si) to extract the effective polarizability from the measurement [132].

4.2 Tip-enhanced infrared spectroscopy

Tip-enhanced infrared spectroscopy is the extension of the s-SNOM scheme by implementing a light source that can access a wide spectral range. Depending on the type of light source, there are two different tip-enhanced IR spectroscopies. The first scheme is swept-IR that uses a tunable IR source for the s-SNOM platform [116–125]. While a continuous-wave tunable laser source is swept over a certain IR range, the reference mirror eliminates background signal either by homodyne [121,123,124] or pseudoheterodyne [125] interferometry. On the other hand, nano-FTIR uses a broadband IR source, such as a difference frequency generation (DFG) laser unit [126–136], global thermal source [137,138], or synchrotron radiation source [139–142]. Recently, another approach has been suggested to use thermal radiation from a heated tip or substrate as a broadband light source in thermal infrared near-field spectroscopy (TINS) [111–113,142–144]. As indicated from its name, nano-FTIR spectroscopy and TINS integrate the FTIR scheme with s-SNOM: the tip-scattered broadband light is interfered with the reference light from the moving reference mirror to generate a temporal interferogram, which provides the IR spectrum of a sample after fast Fourier transform (FFT) analysis. To suppress background signal, the interferogram is demodulated at a higher harmonic oscillation frequency of the AFM cantilever. However, it should be noted that high-harmonic demodulation may not suppress background signal as completely as the homodyne or pseudoheterodyne scheme as discussed earlier.

Tip-enhanced IR spectroscopy was first applied to polar materials, such as SiC and SiO₂, due to high scattering signal upon the excitation of surface phonon polaritons, and have been used as a good benchmark to validate the tip-substrate near-field interaction models [111,116,127]. A planar SiC substrate exhibits a surface phonon polariton (SPhP) resonance at $\sim 948 \text{ cm}^{-1}$ and is therefore excitable at thermal emission wavelengths [157]. This trait of SiC makes it ideally suited for near-field thermal energy conversion devices which can use the resonance to enhance energy transport [7,158,159]. Figure 8 shows the near-field spectra of SiC acquired by swept-IR [116], nano-FTIR [127], and TINS [111], all of which can resolve

the SPhP resonance peak. Figure 8(a) shows the gap dependence of the SPhP resonance for swept-IR spectroscopy, which redshifts up to 15 cm^{-1} as the tip-substrate gap decreases down to 9 nm [116]. A similar redshift behavior is observed in both nano-FTIR and TINS methods. Amarie and Keilmann [127] conducted nano-FTIR spectroscopy measurements for SiC by using a broadband DFG laser source, and observed a $\sim 30 \text{ cm}^{-1}$ redshift of the SPhP resonance: see Fig. 8(b). Additionally, they presented spectra for different demodulation harmonics from $n = 1$ to 3, where the spectra acquired at higher harmonics agree much better with the FDM predictions. Also observed is a sharpening of the measured SiC SPhP resonance with increased harmonic order, which is a direct result of better background suppression at higher harmonics. The TINS results also revealed a large redshift of the SiC SPhP resonance up to 50 cm^{-1} [111] and 60 cm^{-1} [113] (see Fig. 8(c)). The observed spectral redshifts pose a big challenge for the rigorous, quantitative analysis of a material, particularly when its chemo-physical composition is unknown. However, the PDM cannot explain the underlying origin of the spectral redshift. Taubner et al. [116] applied the PDM to interpret their experimental data and found that the PDM could only predict a small redshift ($< 5 \text{ cm}^{-1}$). After all, the PDM is not an adequate model for tip-enhanced IR spectroscopy, as its typical tip-substrate gap distance is much smaller than the minimum gap distance of the PDM. To address this challenge, Amarie and Keilmann [127] applied the FDM to the SiC spectra measured with nano-FTIR. Figure 8(b) shows that the FDM results (solid curves) are in very good agreement with the measurement (solid points). Although not shown here, they also attempted to fit the experimental data with the PDM, but could not make a good agreement. The FDM was further extended to the calculation of near-field thermal radiation in the TINS platform [148]. By combining fluctuation electrodynamics with the FDM framework, they could reproduce a large redshift of the SPhP resonance peak that was observed in the TINS measurement. The good agreement between the FDM and the near-field IR spectrum of SiC reveals that the spectral redshift is due to strong charge interactions between the tip apex and near the surface of the substrate. The amount of the redshift should be sensitive to the tip geometry (i.e., tip radius and tip length) and the tip-substrate separation.

Following the successful tip-enhanced IR spectroscopy of SPhP resonance behaviors, the technique has been applied to study the coupling mechanism of light and electrons through plasmonic resonance excitation. A plasmon is the collective oscillation of an electron cloud in a metallic or semiconductor material, and can be excited by incident radiation [7]. Optically induced plasmonics provide the means to control and manipulate optical fields which is vital for a growing technological transition to light-based communications and information storage

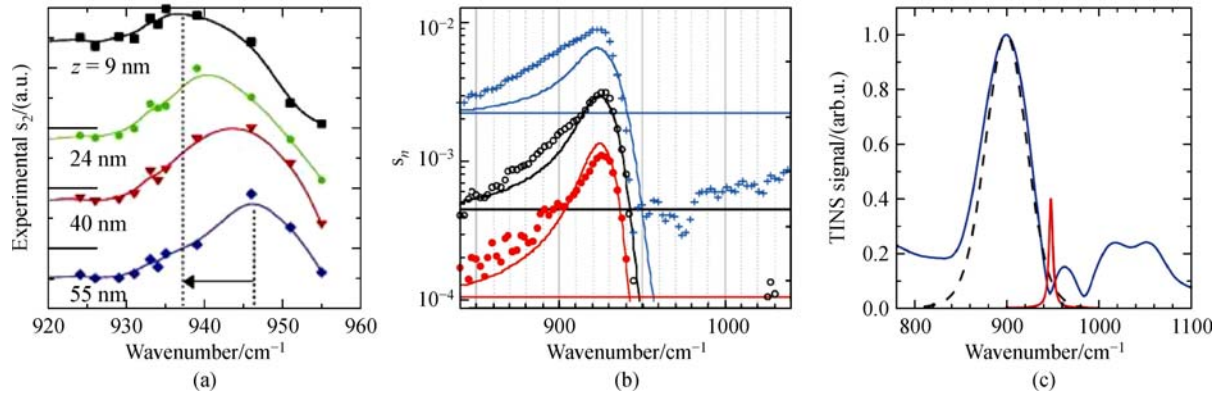


Fig. 8 The surface phonon polariton resonance of SiC probed with tip-enhanced IR spectroscopy [111,116,127]. (a) Swept-IR method showing signal dependence on the tip-substrate separation (solid lines are purely for visual aid) [116]. (b) Nano-FTIR method where the solid lines are the FDM predictions for different tip demodulation harmonics [$n = 1$ (blue), $n = 2$ (black), and $n = 3$ (red)] [127]. (c) TINS method where the blue curve is experimental spectra, the dashed line is a fitted model, and the red curve shows the unshifted resonance position [111]. (a), (b), and (c) adapted with permission from Refs. [116], [127] and [111], respectively. Copyrighted by the (a) American Chemical Society and (b,c) American Physical Society.

technologies [119]. To this end, s-SNOM based spectroscopy can be a critical tool for imaging and characterizing plasmonic resonances observed on nanoantennas [93,108,114,145], nanowires [115], and 2-D materials (e.g., graphene [119,160] and MoS₂ [161]). Shown in Fig. 9(a) are near-field IR spectroscopic images performed on a graphene wedge deposited on a SiC substrate using a swept-IR setup with a grating tunable CO₂ laser [119]. Using the incident IR radiation, plasmons are excited in the graphene wedge, and by increasing the wavelength of the laser, the resonance location of the plasmon moves to a larger geometric constriction. This result confirms the localization of surface plasmons, indicating that the resonant oscillation of electron clouds in graphene is constricted by the geometry of the structure. This is further emphasized in Fig. 9(b), where both the theoretical (blue lines) and experimental (points) results prove the correlation of the plasmon resonance wavelength, which is extracted from the interference fringe separation and/or width of the SNOM image in the graphene wedge, and the wavelength of incident radiation. Figure 9(c) and (d) show another near-field IR spectra taken on a graphene-SiO₂ interface, where the black squares are for bare SiO₂ and the red circles are for the graphene layer on top of SiO₂ [118]. This illustrates that the graphene layer enhances optical scattering of the SPhP with slight blue shift due to strong coupling between the resonant phonons in SiO₂ and mobile carriers in graphene. Their results suggest that graphene can be beneficially used to enhance near-field energy transport in photonic energy conversion devices, such as solar cells and thermophotovoltaic cells.

As previously mentioned in Section 3.2, polymer materials have interesting applications in nanoscale energy systems based on their unique sub-continuum properties to control energy flow due to chain orientation [77,78] and potential applications in thermoelectric conversion [79]. In

addition, far-field IR spectral libraries are well established and provide a reference chemical fingerprint when identifying the local composition of a polymer using its near-field IR spectrum [130]. In Fig. 10, the near-field IR spectra of polymer samples obtained by swept-IR [125], nano-FTIR [130], and TINS [113] are presented with comparisons to far-field or theoretical IR spectra. Each technique turns out to be sensitive to weak molecular vibrational resonances, and the obtained near-field IR spectrum is in good agreement with the far-field counterpart. For weak molecular resonances, tip-enhanced IR spectroscopy does not exhibit the spectral redshift observed when mapping SPhP modes. Figure 10(a) presents near-field IR images and spectra of a PMMA nano-disc around the C=O resonance at 1735 cm⁻¹, measured by the swept-IR scheme with a tunable QCL source [125]. The high power of a QCL allows nanoscopic imaging with a high signal-to-noise ratio, as manifested by the top images. In the bottom plot, IR spectra acquired by swept-IR (solid circles) are compared with the FTIR measurement (black curve) showing good spectral consistency. However, the spectral resolution of swept-IR nanospectroscopy is limited by the linewidth of the laser source, typically worse than that achievable with the nano-FTIR technique. Moreover, QCL power is not uniform over the sweeping wavelength range, often requiring careful calibration at each wavelength with a reference material (Au or Si). This tedious process is the main drawback in achieving a full IR spectrum with the swept-IR method.

Figure 10(b) shows nano-FTIR spectra of 90 nm thick PMMA film when a DFG laser source is used for the spectral range 700 to 1900 cm⁻¹ [130]. The achieved nano-FTIR spectrum is in very good agreement with the transmission-mode FTIR spectrum for a 5- μ m-thick PMMA film in the same spectral range, identifying four

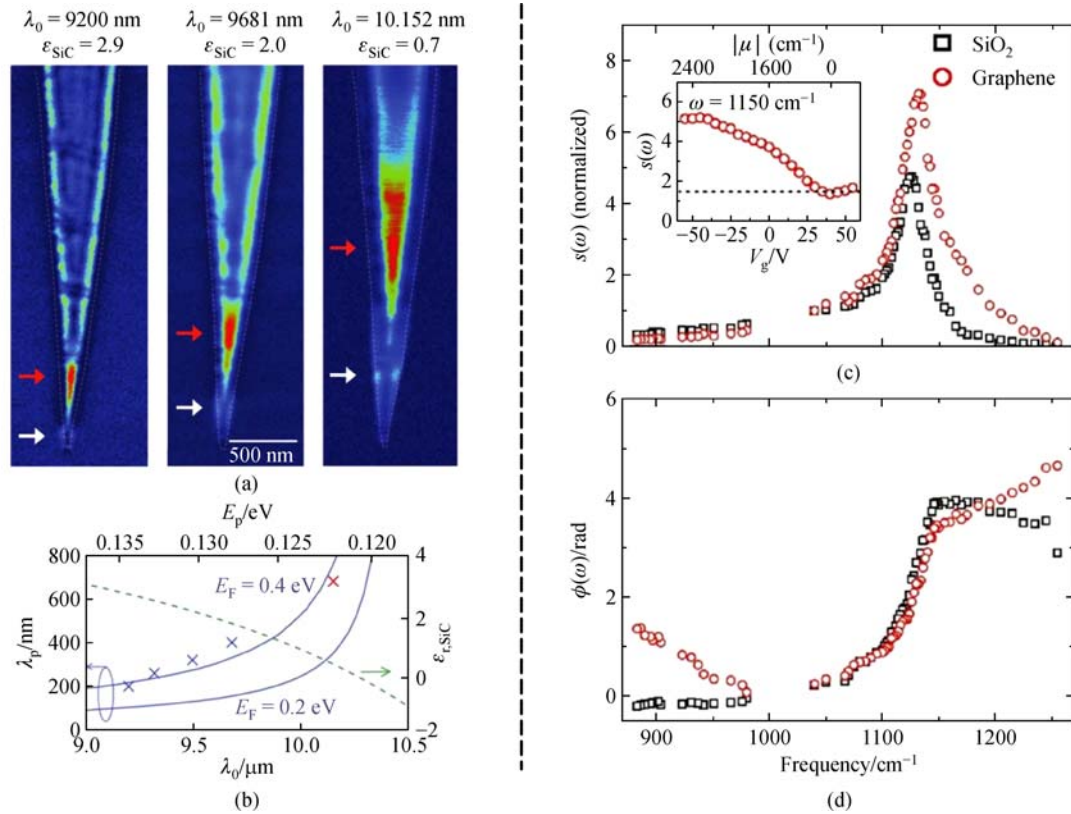


Fig. 9 Nanoscale spectroscopic imaging of graphene plasmons at mid-IR wavelengths using s-SNOM [118,119]. (a) Spectral images of a graphene wedge deposited on SiC taken at different wavelengths ($\lambda_0=9.2, 9.68, 10.15 \mu\text{m}$) [119]. (b) As the geometrical constriction on the graphene wedge increases, the surface plasmon shows localization to require a longer wavelength to be excited. (c) The amplitude and (d) the phase of the near-field IR spectrum on bare SiO₂ (black squares) and a graphene layer on SiO₂ (red circles) [118]. (a, b) and (c, d) adapted with permission from Refs. [118] and [119], respectively. Copyrighted by (a,b) Nature Publishing Group and (c, d) the American Chemical Society.

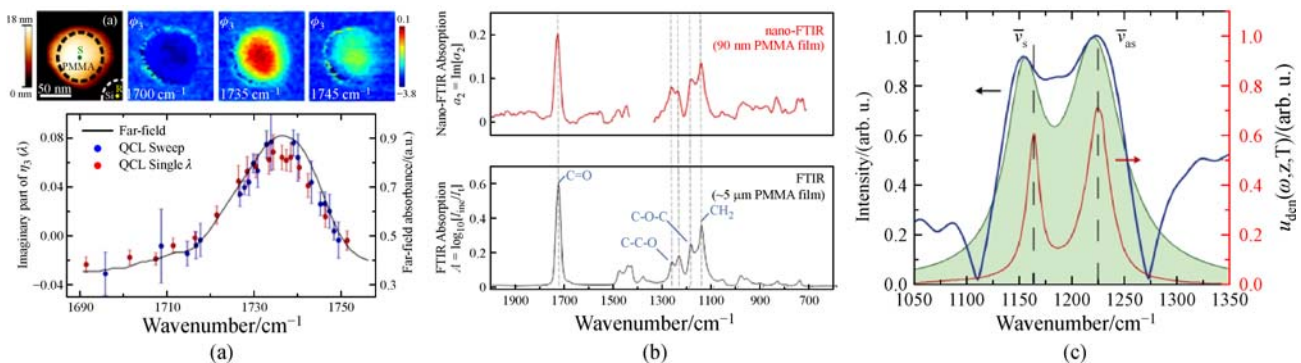


Fig. 10 Weak molecular vibrational resonances of polymers probed with s-SNOM methods [113,125,130]. (a) Swept-IR images (top) and spectrum (bottom) of a PMMA nanodisc. The obtained nano-IR spectrum (solid points) is in good agreement with the far-field FTIR measurement (black curve) [125]. (b) Nano-FTIR spectrum of a PMMA layer (top) in comparison with transmission mode FTIR (bottom) [130]. (c) IR spectrum of a PFTE layer measured by TINS (blue curve) in comparison with the theoretical spectral energy density of near-field radiation (red curve) [113]. (a), (b), and (c) adapted from Refs. [125], [130] and [113], respectively. Copyrighted by the (a) Optical Society of America, (b) American Chemical Society, and (c) Creative Commons Attribution 4.0 International License: Published by AIP Publishing.

major vibrational modes of PMMA (left to right: C = O at 1730 cm⁻¹, C–C–O at 1265 and 1240 cm⁻¹, C–O–C at 1190 cm⁻¹, and CH₂ at 1145 cm⁻¹ [130]). The compelling

advantage of the nano-FTIR scheme is its capability of achieving a continuous, broad-range IR spectrum at the nanoscale. However, the low laser power of a DFG source

(~ 0.25 mW) often requires significant signal integration time to measure a near-field IR spectrum with an acceptable signal-to-noise ratio [130]. This challenge becomes more severe when a globar is used as a cost-effective IR light source [137,138,141]. Synchrotron radiation can significantly enhance the signal-to-noise ratio of nano-FTIR due to its high power, but accessibility to a synchrotron facility is quite limited [141]. The low power throughput radiation is the limiting factor of TINS as well. Although TINS could identify the asymmetric C–F vibrational mode of a polytetrafluoroethylene (PFTE) layer, as shown in Fig. 10(c) [111], thermal radiation emitted from a heated tip is much smaller than the aforementioned light sources and thus may require longer integration time. To address the challenge of using a low power light source, Xu et al. [131] used a broadband femtosecond laser source for nano-FTIR. Using the high energy input of the pulsed laser, they could achieve the nano-FTIR spectrum of a 16 mercaptohexadecanoic-acid (MHDA) monolayer deposited on gold with 25 nm spatial resolution. The obtained signal-to-noise ratio is around 10, which is sufficient to probe 1000 MHDA molecules. This is by far the most sensitive IR spectroscopy measurement, which will open up a great opportunity for single molecular analysis.

Recently, significant efforts have been made to overcome the low power limit of nano-FTIR and to achieve hyperspectral imaging capability. Hyperspectral imaging is a technique that generates a full IR spectrum at each pixel of an image for the complete chemical and structural analysis of heterogeneous materials [4,162,163], suggesting that its scale down to the nanoscale could enable the complete characterization of novel metamaterial structures, polymer blends, nano-composites, and the optimization of nanoscale chemical processes. Figure 11 shows the first successful demonstration of nano-FTIR hyperspectral imaging on a polymer blend, composed of fluorine copolymer (FP), acrylic copolymer (AC), and polystyrene latex (PS), on a silicon substrate [136]. In the figures, the x and y -axis of the 3-dimensional data cubes indicate the scanning directions of the spatial map, while the z -axis provides the spectral variations of each scan over the range of the DFG continuum laser source, 1000–1740 cm^{-1} . The IR spectrum at each pixel reveals the local chemical composition of the sample, yielding spatial resolution as small as 10 nm. For example, Fig. 11(b) shows the spectral slice of the data cube at 1200 cm^{-1} , which clearly identifies the location of FP-rich regions that should have the C–F vibrational resonance at 1195 cm^{-1} . Figure 11(c) provides IR spectra extracted at particular points of the hyperspectral data cube. As indicated by multiple curves, the extracted IR spectra are highly reproducible and identify the dominant polymer component. While curves A and B represent pure PS and AC components, respectively, curves C and D show the blending of AC and FP as indicated by the superposition of signature peaks of both

polymers (i.e., C–F vibration for FP at 1195 cm^{-1} and C=O vibration for AC at 1740 cm^{-1}). Such capability to identify the composition of polymer blends is well demonstrated in Fig. 11(d), which maps the nanoscale distribution of individual polymers by post-processing the extracted IR spectra at each pixel. While the recent progresses in nanoscale hyperspectral IR imaging are remarkable, it is prohibitively tedious to acquire a hyperspectral image and requires demanding post data analysis. For example, the data cube in Fig. 11(a) comprises of 5084 nano-FTIR spectra per image, which took 7.4 h to collect. Such long data acquisition time requires demanding 3-D image processing techniques to compensate the drift of the obtained data during measurement and to stitch overlapping spectral images. The long-operation stabilities of a broadband laser source and a sample scanning stage should be also improved to suppress signal drift.

4.3 Tip-enhanced Raman spectroscopy

Tip-enhanced Raman spectroscopy (TERS) realizes sub-wavelength spatial resolution of Raman spectroscopy by highly concentrating the EM field at the tip apex [21]. The EM field concentration at the tip apex is due to the lightning rod effect [8] and the excitation of surface plasmon polaritons, which can produce a highly enhanced Raman scattering signal. The enhancement factor of TERS can reach 10^7 when a metal-coated tip is brought within one to two nanometers of the sample surface [164]. Therefore, TERS can address the challenging issues of conventional Raman spectroscopy, such as a small scattering cross section and diffraction-limited spatial resolution. The concept of TERS was first proposed in 1985 by Wessel [165] and experimentally realized by several research groups in 2000 [166–169]. Since then, TERS has become a reliable method for label-free, nondestructive nanoscale chemical characterization for biological and crystalline materials [170–172]. TERS has been also extended to hyperspectral imaging [173] and combined with the pump-probe scheme in a stimulated-TERS setup [174].

There are two possible configurations of TERS: reflection mode and transmission mode. In reflection mode, as illustrated by the schematics in Fig. 12, a metallic tip is side-illuminated by a laser source. The scattered light from the surface is collected via the same objective as the excitation source and guided to a photo-spectrometer for the acquisition of the Raman spectrum. While simple to implement, the disadvantage of reflection mode TERS comes from a significant background signal due to the large side-illumination area [175]. In TERS, the far-field background signal cannot be fully suppressed and therefore aggravates the image quality. In transmission mode, the TERS probe is backside-illuminated through the sample using a microscope objective lens, which can focus

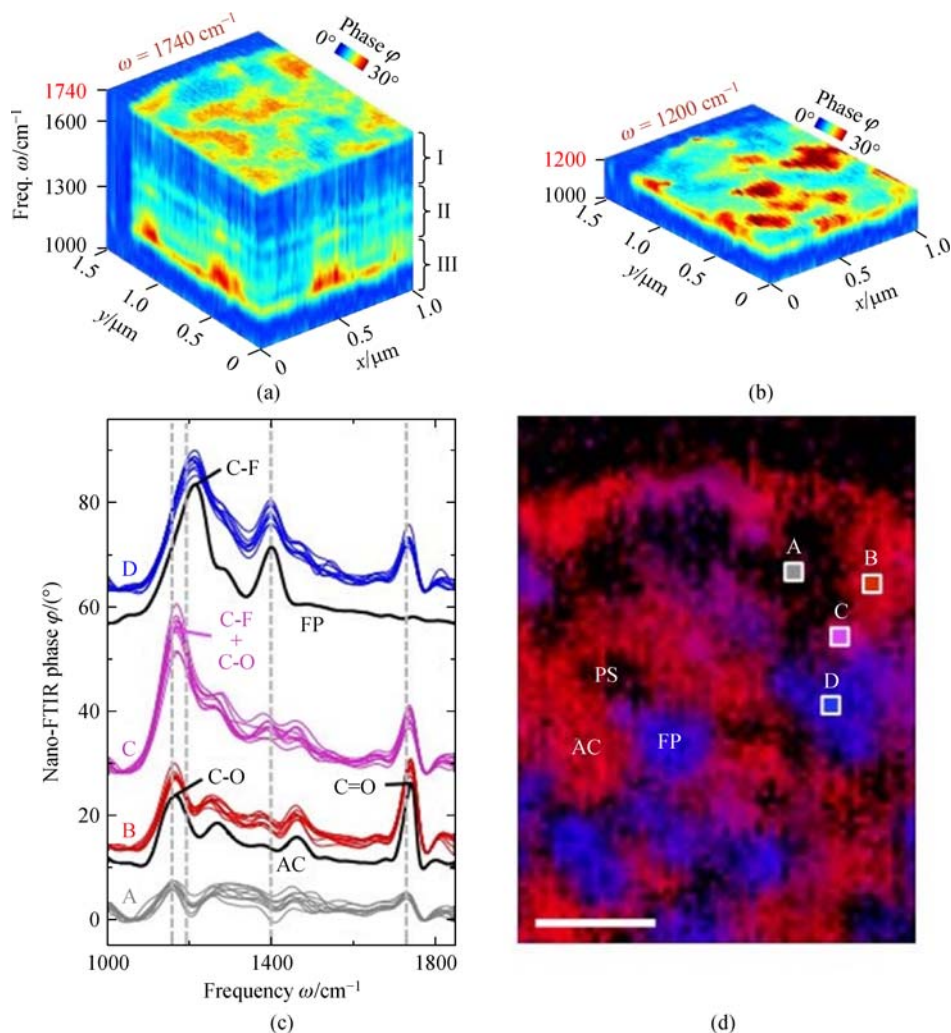


Fig. 11 Nano-FTIR hyperspectral imaging [136]. (a) 3-D hyperspectral image data cube of a fluorine copolymer (FP) - acrylic copolymer (AC) - polystyrene latex (PS) blend on a silicon substrate over the spectral range of 1000–1740 cm^{-1} and (b) its slice at 1200 cm^{-1} to show the FP-rich regions as exhibited by the C–F molecular resonance at 1195 cm^{-1} . (c) The extracted IR spectra are highly reproducible with detailed chemical information of each component. (d) The obtained hyperspectral data can be reproduced to identify the composition of the polymer blend with a nanoscale resolution. Scale bar is 400 nm. Adapted from Ref. [136]. Copyrighted by Creative Commons Attribution 4.0 International License: Published by Nature Publishing Group.

the illuminated spot area around the tip [170]. However, transmission mode TERS only allows probing of transparent samples. Figure 12 also shows the far-field and tip-enhanced Raman spectra of a 30-nm-thick strained silicon (ϵ -Si) layer on $\text{Si}_{0.75}\text{Ge}_{0.25}$ substrate when a silver-coated Si tip is used [176]. The TERS spectrum (red curve) shows the Si-Si phonon mode of the ϵ -Si layer, which cannot be identified by far-field Raman spectroscopy. However, the TERS spectrum also enhances the Si-Si phonon mode in the $\text{Si}_{0.75}\text{Ge}_{0.25}$ substrate and even shows the Si-Si phonon mode in the tip itself. Although the localized EM field at the tip cannot penetrate through the ϵ -Si layer, side-illuminated light reaches to the underlying $\text{Si}_{0.75}\text{Ge}_{0.25}$ substrate and is reflected to interact with the tip. Another noteworthy factor in the enhancement of Raman scattering is the orientation of the vibrational modes: Depending on

the orientation of crystalline or molecular structures, Raman scattering signal may be further enhanced or suppressed [177].

Over the past 10 years, TERS has been intensively used to probe various materials in molecular biology [178–181], chemistry [182,183], and material science [184–187]. Particularly, the remarkable sensitivity of TERS has enabled the spectroscopic imaging of single molecules [188,189]. Figure 13 shows the TERS mapping of a single meso-tetrakis(3,5-di-tertiarybutylphenyl)-porphyrin (H_2TBPP) molecule, clearly visualizing the inner structure and surface configuration of the molecule [189]. For TERS imaging with single-molecule sensitivity, they conducted tunneling-controlled TERS measurements in a cryogenic STM setup. In an ultrahigh vacuum and low temperature (80 K) environment, Raman spectroscopic images with a

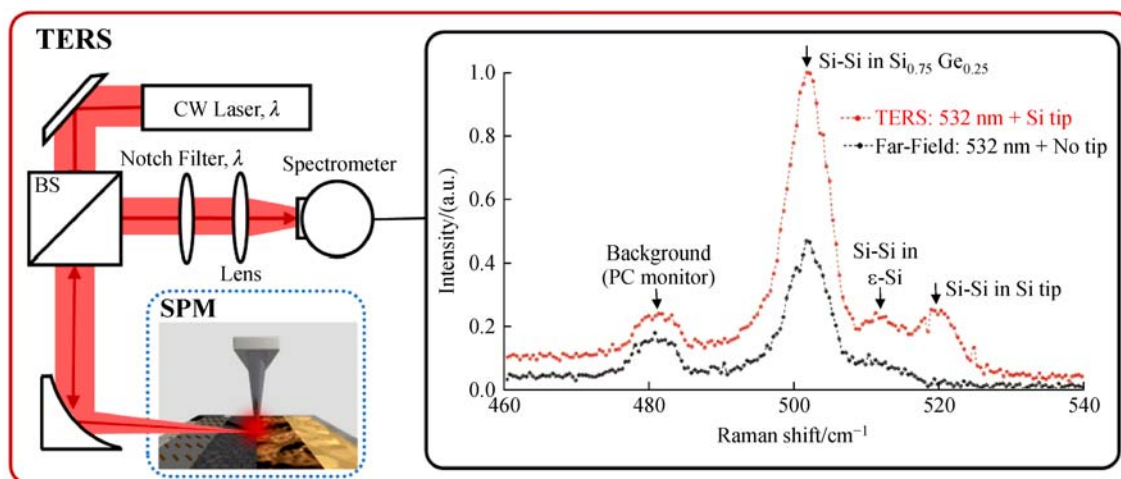


Fig. 12 Reflection mode Tip-enhanced Raman Spectrometer (TERS). Schematic illustration of reflection mode TERS and an example of TERS spectrum for a strained silicon layer on a $\text{Si}_{0.75}\text{Ge}_{0.25}$ substrate. Red curve is obtained by TERS using a Ag-coated Si tip while black curve is the far-field Raman spectrum, both obtained with a 532 nm excitation source [176]. Graph adapted with permission from Ref. [176]. Copyrighted by AIP Publishing.

sub-nanometer resolution were achieved by spectrally matching the nanocavity plasmon resonance between the tip and substrate to the downward molecular vibronic transitions of a H_2TBPP molecule. This spectral matching significantly enhances the emission of Raman photons. Figure 13(a) presents the STM-controlled TERS spectra

when the tip is placed on the lobe (red) and at the center (blue) of the H_2TBPP molecule as well as away from the molecule (black). The TERS spectrum reveals the presence of at least five molecular vibrations when the tip is on the lobe of the molecule which are only marginally visible for the center condition and not visible for bare Ag. The TERS

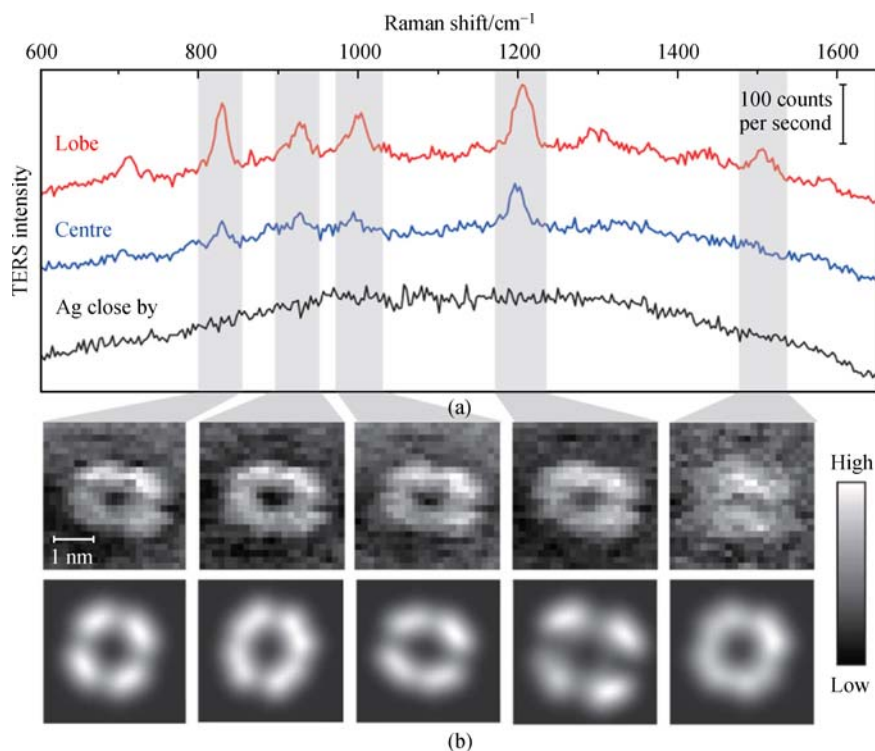


Fig. 13 STM-controlled TERS mapping of a single H_2TBPP molecule [189]. (a) Single molecule TERS spectra on the lobe (red) and center (blue) of a ~ 0.15 nm tall H_2TBPP molecule along with TERS spectrum of bare Ag substrate (black) located 1 nm away from the molecule. (b) Top panel shows the TERS images having a sub-nanometer resolution ($3.6 \text{ nm} \times 3.6 \text{ nm}$ and 23×23 pixels) at different highlighted Raman peaks. Bottom panel shows theoretical simulation of the TERS mapping. Adapted with permission from Ref. [189]. Copyrighted by Nature Publishing Group.

signal of the major vibrational modes are imaged in top portion of Fig. 13(b) and compared with theoretical calculations (bottom). For each vibration mode, the lobes exhibit larger Raman scattering than the center of the molecule. This opens the possibility for imaging single molecule chemical distributions and exciting possibilities in the study of optical processes and photochemistry of single molecules [189].

Although TERS overcomes the limitations of far-field Raman spectroscopy and creates strong opportunities in nanoscale chemical and structural analysis of various materials, tip reproducibility (also referred to as tip yield) [190,191] and the average functional lifespan of the probe [190,192] should be addressed to routinely use TERS with high confidence. The difficulty of tip reproducibility is due to the sensitivity of the plasmonic “hot spot” to minute geometric differences [171]. Significant improvements in tip manufacturing processes have led to reports of nearly 100 percent tip yield [193]. However, the average functional lifespan of a tip has not been improved much. Over the course of several scans, the probe begins to pick up material residues or mechanically break down to degrade the TERS signal. Such tip contamination seriously limits the lifespan of a TERS probe and necessitates the use of ultrahigh vacuum conditions for prolonged use [170].

5 Photo-induced force nanospectroscopy

Photo-induced force microscopy (PiFM) is a novel imaging technique that merges the nanoscale resolution of AFM and the spectroscopic sensitivity of optical

methods by detecting electromagnetically induced forces in an AFM tip-sample junction under laser illumination [194,195]. As shown in Fig. 14(a), PiFM directly measures the electromagnetic force due to the optically induced changes in the dipolar interactions between a sharp polarizable tip and the sample. Therefore, PiFM does not require a complicated light detection scheme, inherently avoiding the overwhelming far-field background signals that plague tip-scattering methods [195,196]. To decouple the photo-induced force from the conservative mechanical forces such as van der Waals and dissipative forces, PiFM is operated either in direct-drive mode or sideband modulation mode [195,197]. In direct-drive mode, the excitation laser modulation (f_m) is typically set at the fundamental mechanical resonance frequency of the cantilever (f_{01}) while the cantilever is mechanically excited at its second mechanical resonance frequency (f_{02}) [195]. This scheme enables readout of the optical interaction at frequency f_{01} while simultaneously measuring the surface topography at frequency f_{02} . However, the disadvantage of direct drive modulation is the convolution of the photo-thermal expansion and the optical dipole-dipole force interaction at the optical excitation frequency. In the sideband-modulation mode, the excitation laser is modulated at the difference between the fundamental and second mechanical resonance frequencies of the cantilever, i.e., $f_m = \Delta f = f_{02} - f_{01}$, such that the optical force is coupled into the fundamental oscillation of the cantilever while the topography is measured at the second cantilever resonance frequency [195,197–199]. With this way, photothermal expansion can be decoupled from the optical force measurement. The bottom images of Fig. 14(a) are the

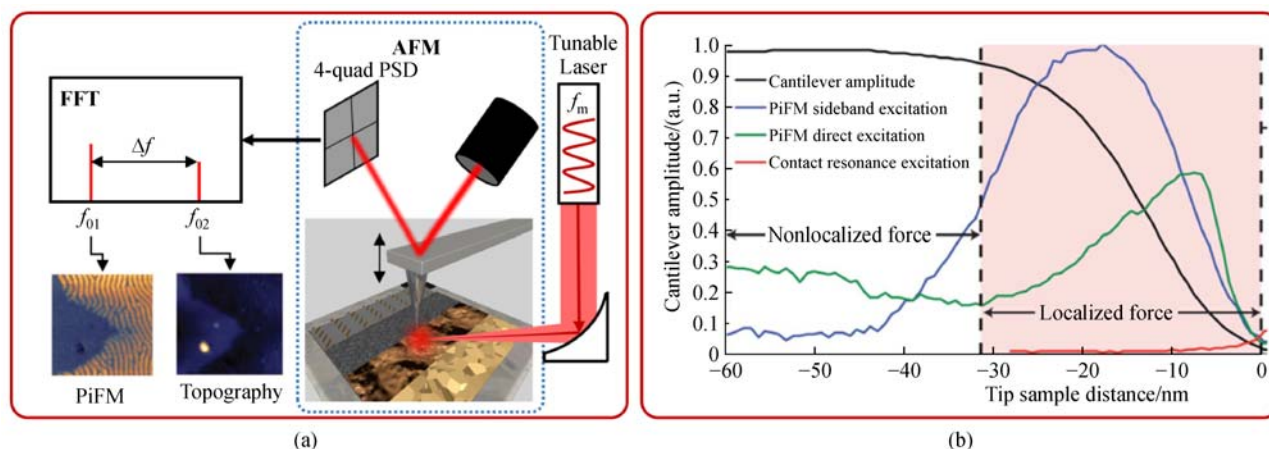


Fig. 14 Photo-induced force microscopy (PiFM). (a) The schematics of PiFM using a 4-quadrant photosensitive detector, where topography is detected at the second mechanical resonance frequency of the cantilever, f_{02} . Optical forces are coupled into the fundamental mechanical resonance of the cantilever, f_{01} , via sideband modulation at $\Delta f = f_{02} - f_{01}$. (b) Cantilever oscillation amplitudes for different modes as function of tip-sample separation when a PS-r-PEDCPMA block copolymer is resonantly excited at 1733 cm^{-1} (i.e., C=O resonance): the topographic cantilever amplitude with f_{02} (black), direct-drive PiFM with $f_m = f_{01}$ (green), sideband modulation PiFM with $f_m = \Delta f$ (blue), and contact resonance excitation (orange). Curves are normalized by the maximum signal obtained in the sideband excitation [195]. (b) adapted with permission from Ref. [195]. Copyrighted under the Creative Commons Attribution 4.0 International License: Published by AAAS.

PiFM and topography images of a poly(styrene-*b*-methyl methacrylate) (PS-*b*-P2VP) block copolymer [195]. While the PS-*b*-P2VP sample has a smooth topography, its PiFM image clearly resolves periodic polystyrene and P2VP domains. While the direct-driven modulation mode is more straightforward to implement, it has been experimentally demonstrated that the sideband excitation results in a larger PiFM signal [195–197]. Figure 14(b) compares the cantilever oscillation amplitudes of the two PiFM modes at 1733 cm^{-1} (i.e., C=O resonance) for a poly(styrene-*r*-epoxydicyclopentadiene methacrylate) (PS-*r*-PEDCPMA) block copolymer, confirming that the sideband modulation induces more cantilever oscillations, approximately twice the oscillation amplitude, than the direct-driven mode. In addition, the sideband modulation decouples the photo-thermal expansion contribution from the photo-induced force measurement [195]. Therefore, PiFM can generate spectroscopic images by sweeping the laser wavelength for a broad range of spectrum [195,197,200]. More discussions on PiFM can be found in Ref. [201]. In the following section, we will discuss the fundamental physics of PiFM and its applications for vibrational nanospectroscopy in more details.

5.1 Basic principles of PiFM

Near-field photo-induced forces detected by PiFM result from complex EM interactions between the tip and sample under the illumination of a diffraction-limited optical field [194]. While a comprehensive understanding of the forces involved requires geometry-dependent numerical simulations, an analytical approximation based on a dipole model can provide qualitative insight into the nature of photo-induced forces [174,194–197,202]. As the simplest model, the tip and a molecule under study can be assumed as spherical point dipoles. When a monochromatic EM wave is incident on the tip-molecule junction, the time-averaged photo-induced force exerted on the tip can be expressed as $\langle \mathbf{F} \rangle = \langle \mathbf{F}_{\text{loc}} \rangle + \langle \mathbf{F}_{\text{nlloc}} \rangle$, where $\langle \mathbf{F}_{\text{loc}} \rangle$ is a localized force, which is dependent on the tip-sample distance, and $\langle \mathbf{F}_{\text{nlloc}} \rangle$ is a non-localized force, which is independent of the tip-sample distance at the nanoscale. Assuming that the tip-molecule separation is greater than the tip radius, the z -component of the local force can be written as [195]

$$\langle F_{\text{loc}} \rangle_z \propto -\frac{1}{z^4} \text{Re}[\alpha_s \alpha_t^*] |E_z|^2 \quad (12)$$

where α_s and α_t are the polarizabilities of the sample molecule and the tip dipole, respectively, and E_z is the z -component of the incident electric field. The z^{-4} gap-dependence defines the highly localized nature of photo-induced forces probed by PiFM [203]. It should be noted that the polarizability is a complex number, i.e., $\alpha_{s(t)} = \alpha'_{s(t)} + i\alpha''_{s(t)}$, and $\alpha_{s(t)}^*$ denotes its complex conjugate. Therefore, $\text{Re}[\alpha_s \alpha_t^*]$ can be rewritten as

$\alpha'_s \alpha'_t + \alpha''_s \alpha''_t$. The role of α_s in Eq. (12) is to carry the spectroscopic information of the sample, and by carefully selecting the tip material such that either α'_t or α''_t is dominant, the PiFM signal can be tuned to measure either the dispersive (real) component, α'_s , or the dissipative (imaginary) component, α''_s , of the sample's polarizability. On the other hand, the nonlocal force can be written as [195]

$$\langle F_{\text{nlloc}} \rangle_z \propto \text{Im}[\alpha_t] |E_x|^2 \quad (13)$$

where E_x is the transverse component of the electric field. From this equation, it is apparent that the nonlocal force does not depend on the tip-sample separation, and it carries no spectral information about the sample. Previous studies have revealed that the localized force component dominates the photo-induced force when the tip-sample separation is less than $\sim 30\text{ nm}$, which is within a typical cantilever oscillation amplitude [195,202].

5.2 PiFM-based vibrational nanospectroscopy

Figure 15(a)–(h) show the first experimental verification of PiFM [196], which recorded topography (a–d) and PiFM (e–h) images of a 6-tamra dye aggregated on a glass slide with four different monochromatic lasers ($\lambda = 475, 543, 594, 633\text{ nm}$). The PiFM results show a clear contrast between the dye and the substrate when the dye is excited at 543 nm and 594 nm while the topographic images show no dependence on the wavelength. The inset in Fig. 15(e) compares the PiFM measurement (square points) with the photoluminescence spectra of the 6-tamra dye measured by a commercial spectrophotometer (solid line). Figure 15(i) is another experimental verification of PiFM that measures the IR spectrum of PMMA using a tunable QCL with spectral range from 800 cm^{-1} to 1800 cm^{-1} [195]. The obtained PiFM IR spectrum is in good agreement with the far-field FTIR measurement (red color), both identifying the C=O resonance at 1735 cm^{-1} . The PiFM spectrum was obtained with a spectral resolution of 1 cm^{-1} and with an integration time of 50 ms at each wavenumber, which is much faster than s-SNOM based nanospectroscopy.

Compared to other techniques reviewed in this paper, PiFM has been recently developed with its first implementation in 2010 [196]. Although the theory and implementation of PiFM has not fully matured, it has been successfully extended to various spectroscopic applications, such as the mapping of near-field optical distributions [198,199,203,204], Raman spectroscopy [197,199,25], dielectric function contrast mapping [199,206], and hyperspectral imaging [195]. Figure 16 shows PiFM images of a PS-*b*-P2VP [poly(styrene-*b*-2-vinyl pyridine)] block copolymer film on a silicon substrate, which are extracted from a 3-dimensional hyperspectral image data cube [195]. The IR spectrum at each pixel was acquired in 400 ms over the spectral range

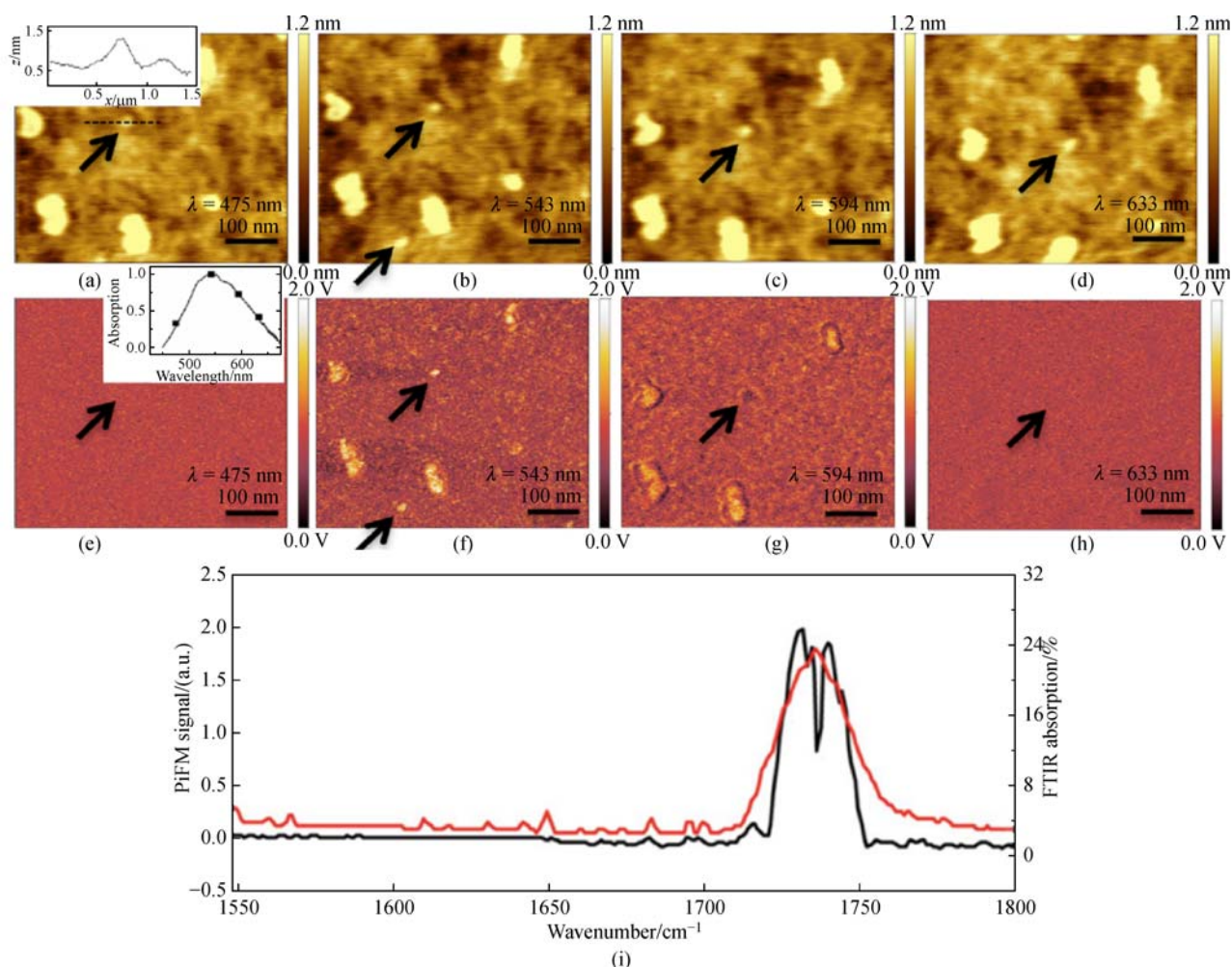


Fig. 15 Experimental verification of PiFM-based nanospectroscopy [195,196]. (a)–(d) Topographical images of 6-tamra dye molecules on glass substrate and (e)–(f) simultaneously recorded PiFM images at different wavelengths ($\lambda = 475, 543, 594, 633$ nm). Inset in (a) is the line profile of a dye island, as indicated by dotted line. Inset in (e) is the spectral data points measured by PiFM which is in good agreement with the photoluminescence spectrum of the dye (solid curve) [196]. (i) Comparison of PiFM-generated IR spectrum (black curve) and the far-field FTIR spectrum (red curve) of a PMMA polymer [195]. (a–h) and (i) Adapted from Refs. [196] and [195], respectively. Copyrighted by (a–h) AIP Publishing and the (i) Creative Commons Attribution 4.0 International License: Published by AAAS.

from 1300 cm^{-1} to 1700 cm^{-1} , which is much faster than the nano-FTIR and TERS hyperspectral imaging techniques. In addition to differentiating the regions of PS and P2VP, the IR spectrum at each pixel in Fig. 16 reveals a third, unknown component. The bottom figure shows the IR spectra extracted from the selected points in Fig. 16(a) and (e), identifying P2VP (red), PS (blue), and P2VP/PS blend (green). Each domain of PS or P2VP is ~ 20 nm wide which demonstrates imaging resolution that surpasses the diffraction limit by more than 100 times [195]. However, due to the immature status of PiFM, it has not been attempted to quantitatively extract the complex optical properties of a material from the measured PiFM spectra. Further development of the background theory and data analysis techniques may be required to fully interpret experimental spectra.

6 Summary and outlook

This article reviews the advances of tip-based vibrational nanospectroscopy to realize non-invasive nanoscale material characterization within many exciting research areas, anticipating that this novel instrumentation will impact the nanoscale analysis of emerging energy materials. Table 1 summarizes the major nanospectroscopy techniques developed to date: PTIR, s-SNOM, TERS, and PiFM. All methods have achieved sub-wavelength spatial resolution in spectroscopic imaging over broad electronic and molecular vibrational resonance ranges while simultaneously acquiring sample topography. Additionally, the acquired spectra are in good agreement with conventional, far-field methods. In general, the methods discussed play more of a complementary role with respect to each other,

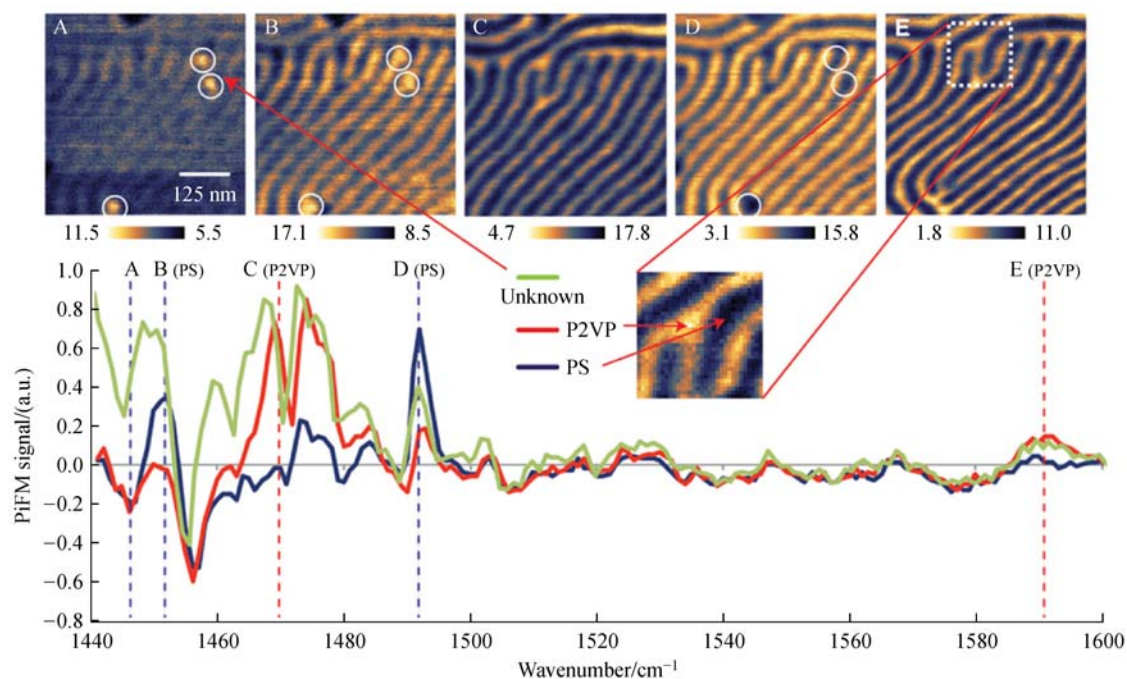


Fig. 16 Hyperspectral nanoscale imaging using PiFM [195]. Spectral images of a PS-*b*-P2VP [poly(styrene-*b*-2-vinyl pyridine)] block copolymer sample at selected wavenumbers: (a) 1447 cm^{-1} (b) 1452 cm^{-1} (c) 1469 cm^{-1} (d) 1492 cm^{-1} , and (e) 1589 cm^{-1} . PiFM spectra are taken from the points in the enlarged section of (e) and the PS/P2VP (green) blend from the bright regions in (a). Adapted from Ref. [195]. Copyrighted under the Creative Commons Attribution 4.0 International License: Published by AAAS.

so a researcher should pay close attention to select a method best suited for their area of interest and personal expertise. PTIR probes a relatively simple mechanism of photothermal absorption, such that the obtained spectra are straight forward to interpret. Thermal expansion PTIR has achieved a sub-20 nm spatial resolution and is routinely used for the study of polymers and biological samples. Furthermore, state-of-the-art PTIR has reached monolayer sensitivity, and can potentially resolve spectra at the atomic scale by integration with STM. However, PTIR cannot easily characterize materials that exhibit low thermal expansion and/or high heat dissipation, preventing in-depth studies of plasmonic metamaterials, SPhP resonances, and 2-D materials. PiFM uses a more conceptually complicated mechanism of optical absorption (photo-induced force). Although PiFM is the least mature of the discussed techniques, great efforts have been instated to bring it onto an equal playing field with its counterpart techniques, including hyperspectral imaging of polymer blend with a 10 nm spatial resolution and imaging of plasmonics structures. Further development of PiFM will cast fundamental insight about optically induced forces and their correlation to molecular and electronic vibrations. However, the origin of the photo-induced force signal has not been clarified and still remains under debate. While thermal expansion induced forces due to the excitation of weak molecular resonances can range from 10 pN–1 nN

and are easily detected by a typical AFM, photo-induced forces due to the same type of resonances are estimated to be in the 1–100 fN range, which would be technically challenging to measure [32,62]. PiFM and PTIR both utilize AFM's superb force detection to generate spectra such that the ultimate sensitivity of these techniques is primarily governed by the sensitivity of the AFM system being used.

In contrast, s-SNOM and TERS optically detect tip-scattered light to measure nanoscale vibrational spectra. They have led scientific breakthroughs in sub-wavelength optical microscopy and spectroscopy, pioneering all major nanospectroscopic characterization regimes, such as hyperspectral imaging, plasmonic mapping, characterization of SPhP resonances, monolayer to single-molecule detection and analysis, and the extraction of nanoscale optical properties. Without question, research using these techniques have made transformative impacts on the understanding of nanoscale light-matter interactions. However, their far reaching impacts do come at a price in that the interpretation of the acquired data are undeniably difficult for the following reasons: overwhelmingly large background signals, difficulty in reproducing results, requirement of precise optical alignment with the AFM tip, and strong coupling of tip and sample optical properties. Many previous studies have aimed to resolve the aforementioned difficulties. However, even after more

Table 1 Summary of tip-based vibrational spectroscopy techniques with pertinent references

	Best spatial resolution/nm	Spectral range /cm ⁻¹	SPhP	Plasmonics	Polymers	Monolayer	Hyperspectral imaging	Optical property extraction	Probe requirement
PTIR	20 [65]	625–6450 [65]	Not yet	Yes [67]	Yes [65]	Yes [62]	Not yet	No	Regular [45]
Thermal expansion	20 [65]	625–6450 [65]	No	Yes [67]	Yes [65]	Yes [62]	No	No	Regular [45]
Temperature rise	500 [39]	700–5000 [39]	No	No	Yes [44]	No	No	No	Functionalized [39]
s-SNOM	20 [130]	700–5000 [141]	Yes [116]	Yes [118]	Yes [125]	Yes [118]	Yes [136]	Yes [132]	Metalized [116]
Swept-IR	25 [125]	880–1800 [118,125]	Yes [116]	Yes [118]	Yes [125]	Yes [118]	Yes [125]	Yes [107]	Metalized [116]
Nano-FTIR	20 [130]	700–5000 [141]	Not yet	Not yet	Yes [130]	Yes [131]	Yes [136]	Yes [132]	Metalized [130]
TINS	50 [143]	780–1800 [113,143]	Yes [111]	No	Yes [113]	No	Yes [142]	Not yet	Typically heated [143]
TERS	<1 [178]		No	No	Yes [175]	Yes [175]	Yes [174]	No	Plasmonic [190]
PiFM	10 [195]	880–1800 [195]	Not yet	Yes [205]	Yes [195]	Not yet	Yes [195]	No	Metalized [195]

than 20 years of efforts, these challenges have not been fully resolved, preventing the routine use of these techniques by inexperienced users.

With the accelerated development of the discussed tip-based vibrational spectroscopy techniques, commercial products that perform one or more of the methods are becoming readily available. *Neaspec GmbH*, the forerunner of s-SNOM, provides several platforms capable of performing swept-IR and nano-FTIR measurements¹⁾. *Anasys Instruments* has pioneered the commercialization of thermal expansion PTIR (referred to by them as AFM-IR) and recently released a new system capable of both PTIR and s-SNOM measurements²⁾. Recently, PiFM in both the visible and IR spectral regions has been commercialized by *Molecular Vista*, combining PiFM with s-SNOM and TERS³⁾. Each system provides probing capabilities of spectral light-matter interactions that can be used for nanoscale material identification, mapping of bonding configurations, and the study material energy properties. In the future, nanomaterials and nanostructures will have significant impact on the advancement of various energy conversion and storage systems, such as solar cells, thermoelectrics, and near-field energy conversion systems, supercapacitors, and batteries. We strongly believe that the commercialization of these techniques will provide user-friendly interfaces for nanoscale vibrational spectroscopy of various energy-related materials, ultimately positioning these instrumentations in the forefront of energy research.

Acknowledgements This work was supported by the National Science Foundation (CBET-1605584) and the University of Utah Funding Incentive

Seed Grant. A.J. also acknowledges financial supports from the University of Utah's Sid Green Fellowship and the National Science Foundation Graduate Research Fellowship (No. 2016213209). C.S. acknowledges financial support from the University of Utah Undergraduate Research Opportunities Program (UROP).

References

- Derrick M, Stulick D, Landry J. Infrared Spectroscopy in Conservation Science. Getty Conservation Institute, USA, 2000
- Griffiths P R, de Haseth J A. Fourier Transform Infrared Spectrometry, 2nd ed. Hoboken: John Wiley and Sons, 2007
- Bhargava R, Ribar T, Koenig J. Towards faster FT-IR imaging by reducing noise. *Applied Spectroscopy*, 1999, 53(11): 1313–1322
- Salzer R, Siesler H W. Infrared and Raman Spectroscopic Imaging. Weinheim: Wiley-VCH, 2009
- Chen G. Nanoscale heat transfer and nanostructured thermoelectrics. *IEEE Transactions on Components, Packaging, and Manufacturing Technology*, 2006, 29(2): 238–246
- Ghashami M, Cho S K, Park K. Near-field enhanced thermionic energy conversion for renewable energy recycling. *Journal of Quantitative Spectroscopy & Radiative Transfer*, 2017, 198: 59–67
- Park K, Zhang Z M. Fundamentals and applications of near-field radiative energy transfer. *Frontiers in Heat & Mass Transfer*, 2013, 4(1): 13001
- Novotny L, Hecht B. Principles of Nano-Optics. Cambridge: Cambridge University Press, 2005
- Zayats A V, Richards D. Nano-optics and Near-field Optical Microscopy. Norwood: Artech House, 2009

1) <http://www.neaspec.com/>

2) <https://www.anasysinstruments.com/>

3) <http://molecularvista.com/>

10. Orrit M. Nobel Prize in chemistry: celebrating optical nanoscopy. *Nature Photonics*, 2014, 8(12): 887–888
11. Bohren C F, Huffman D R. *Absorption and Scattering of Light by Small Particles*. Morlenbach: John Wiley & Sons, 1983
12. Miller L M, Dumas P. Chemical imaging of biological tissue with synchrotron infrared light. *Biochimica et Biophysica Acta*, 2006, 1758(7): 846–857
13. Sullivan D H, Conner W C, Harold M P. Surface analysis with FT-IR emission spectroscopy. *Applied Spectroscopy*, 1992, 46(5): 811–818
14. Globus T R, Woolard D L, Khromova T, Crowe T W, Bykhovskaia M, Gelmont B L, Hesler J, Samuels A C. THz-spectroscopy of biological molecules. *Journal of Biological Physics*, 2003, 29(2–3): 89–100
15. Jin X Y, Kim K J, Lee H S. Grazing incidence reflection absorption Fourier transform infrared (GIRA-FTIR) spectroscopic studies on the ferroelectric behavior of poly(vinylidene fluoride-trifluoroethylene) ultrathin films. *Polymer*, 2005, 46(26): 12410–12415
16. Schliesser A, Brehm M, Keilmann F, van der Weide D. Frequency-comb infrared spectrometer for rapid, remote chemical sensing. *Optics Express*, 2005, 13(22): 9029–9038
17. Nyga P, Drachev V P, Thoreson M D, Shalaev V M. Mid-IR plasmonics and photomodification with Ag films. *Applied Physics B, Lasers and Optics*, 2008, 93(1): 59–68
18. Yu A I T, Pusep A, Milekhin A H. FTIR spectroscopy of longitudinal confined phonons and plasmon-phonon vibrational modes in GaAsn/AlAsm superlattices. *Solid-State Electronics*, 1994, 37(4–6): 613–616
19. Raman C V. A change of wave-length in light scattering. *Nature*, 1928, 121(3051): 619–619
20. Kudelski A. Analytical applications of Raman spectroscopy. *Talanta*, 200, 76(1): 1–8
21. Hayazawa N, Saito Y, Kawata S. Detection and characterization of longitudinal field for tip-enhanced Raman spectroscopy. *Applied Physics Letters*, 2004, 85(25): 6239–6241
22. Efremov E V, Ariese F, Gooijer C. Achievements in resonance Raman spectroscopy: review of a technique with a distinct analytical chemistry potential. *Analytica Chimica Acta*, 2008, 606(2): 119–134
23. Tolles W M, Nibler J W, McDonald J R, Harvey A B. A review of the theory and application of coherent anti-stokes Raman spectroscopy (CARS). *Applied Spectroscopy*, 1977, 31(4): 253–271
24. Fan M, Andrade G F S, Brolo A G. A review on the fabrication of substrates for surface enhanced Raman spectroscopy and their applications in analytical chemistry. *Analytica Chimica Acta*, 2011, 693(1–2): 7–25
25. Rostron P, Gaber S, Gaber D. Raman spectroscopy. *International Journal of Engineering Research and Technology*, 2016, 869(1): 50–64
26. Festy F, Demming A, Richards D. Resonant excitation of tip plasmons for tip-enhanced Raman SNOM. *Ultramicroscopy*, 2004, 100(3–4): 437–441
27. Binnig G, Quate C F, Gerber C. Atomic force microscope. *Physical Review Letters*, 1986, 56(9): 930–933
28. Martin Y, Williams C C, Wickramasinghe H K. Atomic force microscope-force mapping and profiling on a sub 100-nm scale. *Journal of Applied Physics*, 1987, 61(10): 4723–4729
29. Albrecht T R, Quate C F. Atomic resolution imaging of a nonconductor by atomic force microscopy. *Journal of Applied Physics*, 1987, 62(7): 2599–2602
30. Rugar D, Mamin H J, Guethner P. Improved fiber-optic interferometer for atomic force microscopy. *Applied Physics Letters*, 1989, 55(25): 2588–2590
31. Butt H J, Cappella B, Kappl M. Force measurements with the atomic force microscope: technique, interpretation and applications. *Surface Science Reports*, 2005, 59(1–6): 1–152
32. Yang H U, Raschke M B. Resonant optical gradient force interaction for nano-imaging and -spectroscopy. *New Journal of Physics*, 2016, 18(5): 053042
33. Giessibl F J. AFM's path to atomic resolution. *Materials Today*, 2005, 8(5): 32–41
34. Sarid V, Elings V. Review of scanning force microscopy. *Journal of Vacuum Science & Technology B, Nanotechnology and Microelectronics: Materials, Processing, Measurement, and Phenomena*, 1991, 9(2): 431
35. Giessibl F J. Atomic force microscopy in ultrahigh vacuum. *Japanese Journal of Applied Physics*, 1994, 33(6S): 3726–3734
36. Noy A, Vezenov D V, Kayyem J F, Meade T J, Lieber C M. Stretching and breaking duplex DNA by chemical force microscopy. *Chemistry & biology*, 1997, 4(7): 519–527
37. Giessibl F J. Advances in atomic force microscopy. *Reviews of Modern Physics*, 2003, 75(3): 949–983
38. Morita S, Giessibl F, Wiesendanger R. *Noncontact Atomic Force Microscopy*, 2nd ed. Berlin: Springer-Verlag Berlin Heidelberg, 2009
39. Hammiche A, Pollock H M, Reading M, Claybourn M, Turner P H, Jewkes K. Photothermal FT-IR spectroscopy: a step towards FT-IR microscopy at a resolution better than the diffraction limit. *Applied Spectroscopy*, 1999, 53(7): 810–815
40. Bozec L, Hammiche A, Pollock H M, Conroy M, Chalmers J M, Everall N J, Turin L. Localized photothermal infrared spectroscopy using a proximal probe. *Journal of Applied Physics*, 2001, 90(10): 5159–5165
41. Hammiche A, Bozec L, Pollock H M, German M, Reading M. Progress in near-field photothermal infra-red microspectroscopy. *Journal of Microscopy*, 2004, 213(Pt 2): 129–134
42. Majumdar A. Scanning thermal microscopy. *Annual Review of Materials Science*, 1999, 29(1): 505–585
43. Bozec L, Hammiche A, Tobin M, Chalmers J, Everall N, Pollock H. Near-field photothermal Fourier transform infrared spectroscopy using synchrotron radiation. *Measurement Science & Technology*, 2002, 13(8): 1217–1222
44. Donaldson P M, Kelley C S, Frogley M D, Filik J, Wehbe K, Cinque G. Broadband near-field infrared spectromicroscopy using photothermal probes and synchrotron radiation. *Optics Express*, 2016, 24(3): 1852–1864
45. Dazzi A, Prazeres R, Glotin F, Ortega J M. Local infrared microspectroscopy with subwavelength spatial resolution with an atomic force microscope tip used as a photothermal sensor. *Optics Letters*, 2005, 30(18): 2388–2390
46. Dazzi A, Prazeres R, Glotin F, Ortega J M. Subwavelength infrared spectromicroscopy using an AFM as a local absorption sensor.

- Infrared Physics & Technology, 2006, 49(1–2): 113–121
47. Dazzi A, Prazeres R, Glotin F, Ortega J M, Al-Sawaftah M, de Frutos M. Chemical mapping of the distribution of viruses into infected bacteria with a photothermal method. *Ultramicroscopy*, 2008, 108(7): 635–641
 48. Mayet C, Dazzi A, Prazeres R, Allot F, Glotin F, Ortega J M. Sub-100 nm IR spectromicroscopy of living cells. *Optics Letters*, 2008, 33(14): 1611–1613
 49. Houel J, Homeyer E, Sauvage S, Boucaud P, Dazzi A, Prazeres R, Ortéga J M. Midinfrared absorption measured at a $\lambda/400$ resolution with an atomic force microscope. *Optics Express*, 2009, 17(13): 10887–10894
 50. Mayet C, Dazzi A, Prazeres R, Ortega J M, Jaillard D. *In situ* identification and imaging of bacterial polymer nanogranules by infrared nanospectroscopy. *Analyst*, 2010, 135(10): 2540–2545
 51. Prater C, Kjoller K, Cook D, Shetty R, Meyers G, Reinhardt C, Felts J, King W, Vodopyanov K, Dazzi A. Nanoscale infrared spectroscopy of materials by atomic force microscopy. *Microscopy and Analysis (Americas ed.)*, 2010, 24(3): 5–8
 52. Marcott C, Lo M, Kjoller K, Prater C, Noda I. Spatial differentiation of sub-micrometer domains in a poly(hydroxyalkanoate) copolymer using instrumentation that combines atomic force microscopy (AFM) and infrared (IR) spectroscopy. *Applied Spectroscopy*, 2011, 65(10): 1145–1150
 53. Felts J R, Kjoller K, Lo M, Prater C B, King W P. Nanometer-scale infrared spectroscopy of heterogeneous polymer nanostructures fabricated by tip-based nanofabrication. *ACS Nano*, 2012, 6(9): 8015–8021
 54. Lahiri B, Holland G, Centrone A. Chemical imaging beyond the diffraction limit: experimental validation of the PTIR technique. *Small*, 2013, 9(3): 439–445
 55. Felts J R, Kjoller K, Prater C B, King W P. Enhanced nanometer-scale infrared spectroscopy with a contact mode microcantilever having an internal resonator paddle. In: 2010 IEEE 23rd International Conference on Micro Electro Mechanical Systems (MEMS). Hong Kong, China, 2010, 136–139
 56. Policar C, Waern J B, Plamont M A, Clède S, Mayet C, Prazeres R, Ortega J M, Vessières A, Dazzi A. Subcellular IR imaging of a metal-carbonyl moiety using photothermally induced resonance. *Angewandte Chemie (International ed. in English)*, 2011, 50(4): 860–864
 57. Lu F, Belkin M A. Infrared absorption nano-spectroscopy using sample photoexpansion induced by tunable quantum cascade lasers. *Optics Express*, 2011, 19(21): 19942–19947
 58. Dazzi A, Prater C B, Hu Q, Chase D B, Rabolt J F, Marcott C. AFM-IR: combining atomic force microscopy and infrared spectroscopy for nanoscale chemical characterization. *Applied Spectroscopy*, 2012, 66(12): 1365–1384
 59. Kwon B, Schulmerich M V, Elgass L J, Kong R, Holton S E, Bhargava R, King W P. Infrared microspectroscopy combined with conventional atomic force microscopy. *Ultramicroscopy*, 2012, 116: 56–61
 60. Felts J R, Cho H, Yu M F F, Bergman L A, Vakakis A F, King W P. Atomic force microscope infrared spectroscopy on 15 nm scale polymer nanostructures. *Review of Scientific Instruments*, 2013, 84(2): 023709
 61. Cho H, Felts J R, Yu M F, Bergman L A, Vakakis A F, King W P. Improved atomic force microscope infrared spectroscopy for rapid nanometer-scale chemical identification. *Nanotechnology*, 2013, 24(44): 444007
 62. Lu F, Jin M, Belkin M. Tip-enhanced infrared nanospectroscopy via molecular expansion force detection. *Nature Photonics*, 2014, 8(4): 307–312
 63. Felts J R, Law S, Roberts C M, Podolskiy V, Wasserman D M, King W P. Near-field infrared absorption of plasmonic semiconductor microparticles studied using atomic force microscope infrared spectroscopy. *Applied Physics Letters*, 2013, 102(15): 152110
 64. Lahiri B, Holland G, Aksyuk V, Centrone A. Nanoscale imaging of plasmonic hot spots and dark modes with the photothermal-induced resonance technique. *Nano Letters*, 2013, 13(7): 3218–3224
 65. Katzenmeyer A M, Chae J, Kasica R, Holland G, Lahiri B, Centrone A. Nanoscale imaging and spectroscopy of plasmonic modes with the PTIR technique. *Advanced Optical Materials*, 2014, 2(8): 718–722
 66. Katzenmeyer A M, Aksyuk V, Centrone A. Nanoscale infrared spectroscopy: improving the spectral range of the photothermal induced resonance technique. *Analytical Chemistry*, 2013, 85(4): 1972–1979
 67. Katzenmeyer A M, Holland G, Kjoller K, Centrone A. Absorption spectroscopy and imaging from the visible through mid-infrared with 20 nm resolution. *Analytical Chemistry*, 2015, 87(6): 3154–3159
 68. Williams C C, Wickramasinghe H K. Scanning thermal profiler. *Applied Physics Letters*, 1986, 49(23): 1587–1589
 69. Shi L, Majumdar A. Thermal transport mechanisms at nanoscale point contacts. *Journal of Heat Transfer*, 2002, 124(2): 329
 70. Sadat S, Tan A, Chua Y J, Reddy P. Nanoscale thermometry using point contact thermocouples. *Nano Letters*, 2010, 10(7): 2613–2617
 71. Kim K, Jeong W, Lee W, Reddy P. Ultra-high vacuum scanning thermal microscopy for nanometer resolution quantitative thermometry. *ACS Nano*, 2012, 6(5): 4248–4257
 72. Dai Z, King W P, Park K. A 100 nanometer scale resistive heater-thermometer on a silicon cantilever. *Nanotechnology*, 2009, 20(9): 095301
 73. Lee J, Beechem T, Wright T L, Nelson B A, Graham S, King W P. Electrical, thermal, and mechanical characterization of silicon microcantilever heaters. *Journal of Microelectromechanical Systems*, 2006, 15(6): 1644–1655
 74. Corbin E A, Park K, King W P. Room-temperature temperature sensitivity and resolution of doped-silicon microcantilevers. *Applied Physics Letters*, 2009, 94(24): 243503
 75. Dazzi A, Glotin F, Carminati R. Theory of infrared nanospectroscopy by photothermal induced resonance. *Journal of Applied Physics*, 2010, 107(12): 124519
 76. Pechenezhskiy I V, Hong X, Nguyen G D, Dahl J E P, Carlson R M K, Wang F, Crommie M F. Infrared spectroscopy of molecular submonolayers on surfaces by infrared scanning tunneling microscopy: tetramantane on Au(111). *Physical Review Letters*, 2013, 111(12): 126101

77. Nguyen T Q, Wu J, Tolbert S H, Schwartz B J. Control of energy transport in conjugated polymers using an ordered mesoporous silica matrix. *Advanced Materials*, 2001, 13(8): 609–611
78. Luo T, Chen G. Nanoscale heat transfer—from computation to experiment. *Physical chemistry chemical physics : PCCP*, 2013, 15(10): 3389–3412
79. Wang Y, Liu J, Zhou J, Yang R. Thermoelectric transport across nanoscale polymer–semiconductor–polymer junctions. *Journal of Physical Chemistry C*, 2013, 117(47): 24716–24725
80. Merklin G T, He L, Griffiths P R. Surface-enhanced infrared absorption spectrometry of p-nitrothiophenol and its disulfide. *Applied Spectroscopy*, 1999, 53(11): 1448–1453
81. Pohl D W, Denk W, Lanz M. Optical stethoscopy: image recording with resolution $\lambda/20$. *Applied Physics Letters*, 1984, 44(7): 651–653
82. Betzig E, Lewis A, Harootunian A, Isaacson M, Kratschmer E. Near field scanning optical microscopy (NSOM): development and biophysical applications. *Biophysical Journal*, 1986, 49(1): 269–279
83. Labardi M, Gucciardi P G, Allegrini M, Pelosi C. Assessment of NSOM resolution on III–V semiconductor thin films. *Applied Physics. A, Materials Science & Processing*, 1998, 66(S1): S397–S402
84. Isaacson M. Near-field scanning optical microscopy II. *Journal of Vacuum Science and Technology. B, Nanotechnology & Microelectronics: Materials, Processing, Measurement, & Phenomena: JVST B*, 1991, 9(6): 3103
85. Goodson K E, Ashegh M. Near-field optical thermometry. *Microscale Thermophysical Engineering*, 1997, 1(3): 225–235
86. Sasaki M, Tanaka K, Hane K. Cantilever probe integrated with light-emitting diode, waveguide, aperture, and photodiode for scanning near-field optical microscope. *Japan Society of Applied Physics*, 2000, 39(12B): 7150–7153
87. Michaelis J, Hettich C, Mlynek J, Sandoghdar V V. Optical microscopy using a single-molecule light source. *Nature*, 2000, 405(6784): 325–328
88. Shubeita G T, Sekatskii S K, Dietler G, Potapova I, Mews A, Basché T. Scanning near-field optical microscopy using semiconductor nanocrystals as a local fluorescence and fluorescence resonance energy transfer source. *Journal of Microscopy*, 2003, 210(Pt 3): 274–278
89. Chevalier N, Nasse M J, Woehl J C, Reiss P, Bleuse J, Chandezon F, Huant S. CdSe single-nanoparticle based active tips for near-field optical microscopy. *Nanotechnology*, 2005, 16(4): 613–618
90. Kim J, Song K B. Recent progress of nano-technology with NSOM. *Micron (Oxford, England)*, 1993, 2007, 38(4): 409–426
91. Mauser N, Hartschuh A. Tip-enhanced near-field optical microscopy. *Chemical Society Reviews*, 2014, 43(4): 1248–1262
92. Hartschuh A. Tip-enhanced near-field optical microscopy. *Angewandte Chemie (International ed. in English)*, 2008, 47(43): 8178–8191
93. Neuman T, Alonso-González P, Garcia-Etxarri A, Schnell M, Hillenbrand R, Aizpurua J. Mapping the near fields of plasmonic nanoantennas by scattering-type scanning near-field optical microscopy. *Laser & Photonics Reviews*, 2015, 9(6): 637–649
94. Novotny L, Stranick S J. Near-field optical microscopy and spectroscopy with pointed probes. *Annual Review of Physical Chemistry*, 2006, 57(1): 303–331
95. Lucas M, Riedo E. Invited review article: combining scanning probe microscopy with optical spectroscopy for applications in biology and materials science. *The Review of Scientific Instruments*, 2012, 83(6): 061101
96. Hillenbrand R, Keilmann F. Complex optical constants on a subwavelength scale. *Physical Review Letters*, 2000, 85(14): 3029–3032
97. Yang T J, Lessard G A, Quake S R. An apertureless near-field microscope for fluorescence imaging. *Applied Physics Letters*, 2000, 76(3): 378–380
98. Labardi M, Tikhomirov O, Ascoli C, Allegrini M. Balanced homodyne for apertureless near-field optical imaging. *The Review of Scientific Instruments*, 2008, 79(3): 033709
99. Gomez L, Bachelot R, Bouhelier A, Wiederrecht G P, Chang S H, Gray S K, Hua F, Jeon S, Rogers J A, Castro M E, Blaize S, Stefanon I, Lerondel G, Royer P. Apertureless scanning near-field optical microscopy: a comparison between homodyne and heterodyne approaches. *Journal of the Optical Society of America. B, Optical Physics*, 2006, 23(5): 823
100. Taubner T, Hillenbrand R, Keilmann F. Performance of visible and mid-infrared scattering-type near-field optical microscopes. *Journal of Microscopy*, 2003, 210(Pt 3): 311–314
101. Hillenbrand R, Knoll B, Keilmann F. Pure optical contrast in scattering-type scanning near-field microscopy. *Journal of Microscopy*, 2001, 202(Pt 1): 77–83
102. Raschke M B, Lienau C. Apertureless near-field optical microscopy: tip–sample coupling in elastic light scattering. *Applied Physics Letters*, 2003, 83(24): 5089–5091
103. Knoll B, Keilmann F. Near-field probing of vibrational absorption for chemical microscopy. *Nature*, 1999, 399(6732): 134–137
104. Knoll B, Keilmann F. Enhanced dielectric contrast in scattering-type scanning near-field optical microscopy. *Optics Communications*, 2000, 182(4–6): 321–328
105. Hillenbrand R, Taubner T, Keilmann F. Phonon-enhanced light matter interaction at the nanometre scale. *Nature*, 2002, 418(6894): 159–162
106. Ocelic N, Huber A, Hillenbrand R. Pseudoheterodyne detection for background-free near-field spectroscopy. *Applied Physics Letters*, 2006, 89(10): 101124
107. Ocelic N. Quantitative near-field phonon-polariton spectroscopy. Dissertation for the Doctoral Degree. Munich: Technical University of Munich, 2007
108. Schnell M, Carney P S, Hillenbrand R. Synthetic optical holography for rapid nanoimaging. *Nature Communications*, 2014, 5: 3499
109. Deutsch B, Hillenbrand R, Novotny L. Near-field amplitude and phase recovery using phase-shifting interferometry. *Optics Express*, 2008, 16(2): 494–501
110. Huber A J, Keilmann F, Wittborn J, Aizpurua J, Hillenbrand R. Terahertz near-field nanoscopy of mobile carriers in single semiconductor nanodevices. *Nano Letters*, 2008, 8(11): 3766–3770
111. O’Callahan B T, Lewis W E, Jones A C, Raschke M B. Spectral frustration and spatial coherence in thermal near-field spectro-

- scopy. *Physical Review B: Condensed Matter and Materials Physics*, 2014, 89(24): 245446
112. Babuty A, Joulain K, Chapuis P O, Greffet J J, De Wilde Y. Blackbody spectrum revisited in the near field. *Physical Review Letters*, 2013, 110(14): 146103
113. O'Callahan B T, Raschke M B. Laser heating of scanning probe tips for thermal near-field spectroscopy and imaging. *APL Photonics*, 2017, 2(2):021301
114. Schnell M, García-Etxarri A, Huber A J, Crozier K, Aizpurua J, Hillenbrand R. Controlling the near-field oscillations of loaded plasmonic nanoantennas. *Nature Photonics*, 2009, 3(5): 287–291
115. Jones A C, Olmon R L, Skrabalak S E, Wiley B J, Xia Y N, Raschke M B. Mid-IR plasmonics: near-field imaging of coherent plasmon modes of silver nanowires. *Nano Letters*, 2009, 9(7): 2553–2558
116. Taubner T, Keilmann F, Hillenbrand R. Nanomechanical resonance tuning and phase effects in optical near-field interaction. *Nano Letters*, 2004, 4(9): 1669–1672
117. Zhang L M, Andreev G O, Fei Z, McLeod A S, Dominguez G, Thiemens M, Castro-Neto A H, Basov D N, Fogler M M. Near-field spectroscopy of silicon dioxide thin films. *Physical Review B: Condensed Matter and Materials Physics*, 2012, 85(7): 075419
118. Fei Z, Andreev G O, Bao W, Zhang L M, McLeod A S, Wang C, Stewart M K, Zhao Z, Dominguez G, Thiemens M, Fogler M M, Tauber M J, Castro-Neto A H, Lau C N, Keilmann F, Basov D N. Infrared nanoscopy of dirac plasmons at the graphene-SiO₂ interface. *Nano Letters*, 2011, 11(11): 4701–4705
119. Chen J, Badioli M, Alonso-González P, Thongrattanasiri S, Huth F, Osmond J, Spasenović M, Centeno A, Pesquera A, Godignon P, Elorza A Z, Camara N, García de Abajo F J, Hillenbrand R, Koppens F H. Optical nano-imaging of gate-tunable graphene plasmons. *Nature*, 2012, 487(7405): 77–81
120. Huth F, Chuvilin A, Schnell M, Amenabar I, Krutokhvostov R, Lopatin S, Hillenbrand R. Resonant antenna probes for tip-enhanced infrared near-field microscopy. *Nano Letters*, 2013, 13(3): 1065–1072
121. Xu X G, Tanur A E, Walker G C. Phase controlled homodyne infrared near-field microscopy and spectroscopy reveal inhomogeneity within and among individual boron nitride nanotubes. *Journal of Physical Chemistry A*, 2013, 117(16): 3348–3354
122. Fei Z, Rodin A S, Gannett W, Dai S, Regan W, Wagner M, Liu M K, McLeod A S, Dominguez G, Thiemens M, Castro Neto A H, Keilmann F, Zettl A, Hillenbrand R, Fogler M M, Basov D N. Electronic and plasmonic phenomena at graphene grain boundaries. *Nature Nanotechnology*, 2013, 8(11): 821–825
123. Berweger S, Nguyen D M, Muller E A, Bechtel H A, Perkins T T, Raschke M B. Nano-chemical infrared imaging of membrane proteins in lipid bilayers. *Journal of the American Chemical Society*, 2013, 135(49): 18292–18295
124. Xu X G, Gilburd L, Walker G C. Phase stabilized homodyne of infrared scattering type scanning near-field optical microscopy. *Applied Physics Letters*, 2014, 105(26): 263104
125. Yoxall E, Schnell M, Mastel S, Hillenbrand R. Magnitude and phase-resolved infrared vibrational nanospectroscopy with a swept quantum cascade laser. *Optics Express*, 2015, 23(10): 13358–13369
126. Amarie S, Ganz T, Keilmann F. Mid-infrared near-field spectroscopy. *Optics Express*, 2009, 17(24): 21794–21801
127. Amarie S, Keilmann F. Broadband-infrared assessment of phonon resonance in scattering-type near-field microscopy. *Physical Review B: Condensed Matter and Materials Physics*, 2011, 83(4): 045404
128. Keilmann F, Amarie S. Mid-infrared frequency comb spanning an octave based on an Er fiber laser and difference-frequency generation. *Journal of Infrared, Millimeter and Terahertz Waves*, 2012, 33(5): 479–484
129. Amarie S, Zaslansky P, Kajihara Y, Griesshaber E, Schmahl W W, Keilmann F. Nano-FTIR chemical mapping of minerals in biological materials. *Beilstein Journal of Nanotechnology*, 2012, 3: 312–323
130. Huth F, Govyadinov A, Amarie S, Nuansing W, Keilmann F, Hillenbrand R. Nano-FTIR absorption spectroscopy of molecular fingerprints at 20 nm spatial resolution. *Nano Letters*, 2012, 12(8): 3973–3978
131. Xu X G, Rang M, Craig I M, Raschke M B. Pushing the sample-size limit of infrared vibrational nanospectroscopy: from monolayer toward single molecule sensitivity. *The Journal of Physical Chemistry Letters*, 2012, 3(13): 1836–1841
132. Govyadinov A A, Amenabar I, Huth F, Carney P S, Hillenbrand R. Quantitative measurement of local infrared absorption and dielectric function with tip-enhanced near-field microscopy. *The Journal of Physical Chemistry Letters*, 2013, 4(9): 1526–1531
133. Amenabar I, Poly S, Nuansing W, Hubrich E H, Govyadinov A A, Huth F, Krutokhvostov R, Zhang L, Knez M, Heberle J, Bittner A M, Hillenbrand R. Structural analysis and mapping of individual protein complexes by infrared nanospectroscopy. *Nature Communications*, 2013, 4: 2890
134. McLeod A S, Kelly P, Goldflam M D, Gainsforth Z, Westphal A J, Dominguez G, Thiemens M H, Fogler M M, Basov D N. Model for quantitative tip-enhanced spectroscopy and the extraction of nanoscale-resolved optical constants. *Physical Review B: Condensed Matter and Materials Physics*, 2014, 90(8): 085136
135. Khatib O, Wood J D, McLeod A S, Goldflam M D, Wagner M, Damhorst G L, Koepke J C, Doidge G P, Rangarajan A, Bashir R, Pop E, Lyding J W, Thiemens M H, Keilmann F, Basov D N. Graphene-based platform for infrared near-field nanospectroscopy of water and biological materials in an aqueous environment. *ACS Nano*, 2015, 9(8): 7968–7975
136. Amenabar I, Poly S, Goikoetxea M, Nuansing W, Lasch P, Hillenbrand R. Hyperspectral infrared nanoimaging of organic samples based on Fourier transform infrared nanospectroscopy. *Nature Communications*, 2017, 8: 14402
137. Huth F, Schnell M, Wittborn J, Ocelic N, Hillenbrand R. Infrared-spectroscopic nanoimaging with a thermal source. *Nature Materials*, 2011, 10(5): 352–356
138. O'Callahan B T, Lewis W E, Möbius S, Stanley J C, Muller E A, Raschke M B. Broadband infrared vibrational nano-spectroscopy using thermal blackbody radiation. *Optics Express*, 2015, 23(25): 32063–32074
139. Ikemoto Y, Ishikawa M, Nakashima S, Okamura H, Haruyama Y, Matsui S, Moriwaki T, Kinoshita T. Development of scattering near-field optical microspectroscopy apparatus using an infrared

- synchrotron radiation source. *Optics Communications*, 2012, 285 (8): 2212–2217
140. Hermann P, Hoehl A, Patoka P, Huth F, Rühl E, Ulm G. Near-field imaging and nano-Fourier-transform infrared spectroscopy using broadband synchrotron radiation. *Optics Express*, 2013, 21(3): 2913–2919
141. Bechtel H A, Muller E A, Olmon R L, Martin M C, Raschke M B. Ultrabroadband infrared nanospectroscopic imaging. *Proceedings of the National Academy of Sciences of the United States of America*, 2014, 111(20): 7191–7196
142. Peragut F, Brubach J B, Roy P, de Wilde Y. Infrared near-field imaging and spectroscopy based on thermal or synchrotron radiation. *Applied Physics Letters*, 2014, 104(25): 251118
143. Jones A C, Raschke M B. Thermal infrared near-field spectroscopy. *Nano Letters*, 2012, 12(3): 1475–1481
144. Jones A C, O’Callahan B T, Yang H U, Raschke M B. The thermal near-field: coherence, spectroscopy, heat-transfer, and optical forces. *Progress in Surface Science*, 2013, 88(4): 349–392
145. Alonso-González P, Albella P, Neubrech F, Huck C, Chen J, Golmar F, Casanova F, Hueso L E, Pucci A, Aizpurua J, Hillenbrand R. Experimental verification of the spectral shift between near- and far-field peak intensities of plasmonic infrared nanoantennas. *Physical Review Letters*, 2013, 110(20): 203902
146. Walford J N, Porto J A, Carminati R, Greffet J J, Adam P M, Hudlet S, Bijeon J L, Stashkevich A, Royer P. Influence of tip modulation on image formation in scanning near-field optical microscopy. *Journal of Applied Physics*, 2001, 89(9): 5159–5169
147. Joulain K, Ben-Abdallah P, Chapuis P O, de Wilde Y, Babuty A, Henkel C. Strong tip-sample coupling in thermal radiation scanning tunneling microscopy. *Journal of Quantitative Spectroscopy & Radiative Transfer*, 2014, 136: 1–15
148. Jarzembski A, Park K. Finite dipole model for extreme near-field thermal radiation between a tip and planar SiC substrate. *Journal of Quantitative Spectroscopy & Radiative Transfer*, 2017, 191: 67–74
149. Cvitkovic A, Ocelic N, Hillenbrand R. Analytical model for quantitative prediction of material contrasts in scattering-type near-field optical microscopy. *Optics Express*, 2007, 15(14): 8550–8565
150. Cvitkovic A, Ocelic N, Aizpurua J, Guckenberger R, Hillenbrand R. Infrared imaging of single nanoparticles via strong field enhancement in a scanning nanogap. *Physical Review Letters*, 2006, 97(6): 060801
151. Renger J, Grafström S, Eng L M, Hillenbrand R. Resonant light scattering by near-field-induced phonon polaritons. *Physical Review B: Condensed Matter and Materials Physics*, 2005, 71 (7): 075410
152. Fikri R, Barchiesi D, H’Dhili F, Bachelot R, Vial A, Royer P. Modeling recent experiments of apertureless near-field optical microscopy using 2D finite element method. *Optics Communications*, 2003, 221(1–3): 13–22
153. Micic M, Klymyshyn N, Suh Y, Lu H. Finite element method simulation of the field distribution for AFM tip-enhanced surface-enhanced Raman scanning microscopy. *Journal of Physical Chemistry B*, 2003, 107(7): 1574–1584
154. Brehm M, Schliesser A, Cajko F, Tsukerman I, Keilmann F. Antenna-mediated back-scattering efficiency in infrared near-field microscopy. *Optics Express*, 2008, 16(15): 11203–11215
155. Sukhov S V. Role of multipole moment of the probe in apertureless near-field optical microscopy. *Ultramicroscopy*, 2004, 101(2–4): 111–122
156. Hatano H, Kawata S. Applicability of deconvolution and nonlinear optimization for reconstructing optical images from near-field optical microscope images. *Journal of Microscopy*, 1999, 194(2–3): 230–234
157. Zhang Z M. *Nano/microscale Heat Transfer*, 5th ed. New York: McGraw Hill, 2007
158. Lee B J, Park K, Zhang Z M. Energy pathways in nanoscale thermal radiation. *Applied Physics Letters*, 2007, 91(15): 153101
159. Francoeur M, Basu S, Petersen S J. Electric and magnetic surface polariton mediated near-field radiative heat transfer between metamaterials made of silicon carbide particles. *Optics Express*, 2011, 19(20): 18774–18788
160. Fei Z, Rodin A S, Andreev G O, Bao W, McLeod A S, Wagner M, Zhang L M, Zhao Z, Thiemens M, Dominguez G, Fogler M M, Castro Neto A H, Lau C N, Keilmann F, Basov D N. Gate-tuning of graphene plasmons revealed by infrared nano-imaging. *Nature*, 2012, 487(7405): 82–85
161. Wang Q H, Kalantar-Zadeh K, Kis A, Coleman J N, Strano M S. Electronics and optoelectronics of two-dimensional transition metal dichalcogenides. *Nature Nanotechnology*, 2012, 7(11): 699–712
162. Gowen A A, O’Donnell C P, Cullen P J, Downey G, Frias J M. Hyperspectral imaging—an emerging process analytical tool for food quality and safety control. *Trends in Food Science & Technology*, 2007, 18(12): 590–598
163. Lu G, Fei B. Medical hyperspectral imaging: a review. *Journal of Biomedical Optics*, 2014, 19(1): 010901
164. Ossikovski R, Nguyen Q, Picardi G. Simple model for the polarization effects in tip-enhanced Raman spectroscopy. *Physical Review B: Condensed Matter and Materials Physics*, 2007, 75(4): 045412
165. Wessel J. Surface-enhanced optical microscopy. *Journal of the Optical Society of America. B, Optical Physics*, 1985, 2(9): 1538
166. Stöckle R M, Suh Y D, Deckert V, Zenobi R. Nanoscale chemical analysis by tip-enhanced Raman spectroscopy. *Chemical Physics Letters*, 2000, 318(1–3): 131–136
167. Hayazawa N, Inouye Y, Sekkat Z, Kawata S. Metallized tip amplification of near-field Raman scattering. *Optics Communications*, 2000, 183(1–4): 333–336
168. Anderson M S. Locally enhanced Raman spectroscopy with an atomic force microscope. *Applied Physics Letters*, 2000, 76(21): 3130–3132
169. Pettinger B, Picardi G, Schuster R, Ertl G. Surface enhanced Raman spectroscopy: towards single molecular spectroscopy. *Electrochemistry*, 2000, 68(12): 942–949
170. Bailo E, Deckert V. Tip-enhanced Raman scattering. *Chemical Society Reviews*, 2008, 37(5): 921–930
171. Yeo B S, Stadler J, Schmid T, Zenobi R, Zhang W. Tip-enhanced Raman Spectroscopy—its status, challenges and future directions. *Chemical Physics Letters*, 2009, 472(1–3): 1–13
172. Kumar N, Mignuzzi S, Su W, Roy D. Tip-enhanced Raman spectroscopy: principles and applications. *EPJ Techniques and Instrumentation*, 2015, 2(1): 9

173. Weber-Bargioni A, Schwartzberg A, Cornaglia M, Ismach A, Urban J J, Pang Y, Gordon R, Bokor J, Salmeron M B, Ogletree D F, Ashby P, Cabrini S, Schuck P J. Hyperspectral nanoscale imaging on dielectric substrates with coaxial optical antenna scan probes. *Nano Letters*, 2011, 11(3): 1201–1207
174. Wickramasinghe H K, Chaigneau M, Yasukuni R, Picardi G, Ossikovski R. Billion-fold increase in tip-enhanced Raman signal. *ACS Nano*, 2014, 8(4): 3421–3426
175. Sackrow M, Stanciu C, Lieb M A, Meixner A J. Imaging nanometre-sized hot spots on smooth Au films with high-resolution tip-enhanced luminescence and Raman near-field optical microscopy. *Chemphyschem*, 2008, 9(2): 316–320
176. Tarun A, Hayazawa N, Motohashi M, Kawata S. Highly efficient tip-enhanced Raman spectroscopy and microscopy of strained silicon. *Review of Scientific Instruments*, 2008, 79(1): 013706
177. Saito Y, Hayazawa N, Kataura H, Murakami T, Tsukagoshi K, Inouye Y, Kawata S. Polarization measurements in tip-enhanced Raman spectroscopy applied to single-walled carbon nanotubes. *Chemical Physics Letters*, 2005, 410(1–3): 136–141
178. Neugebauer U, Rösch P, Schmitt M, Popp J, Julien C, Rasmussen A, Budich C, Deckert V. On the way to nanometer-sized information of the bacterial surface by tip-enhanced Raman spectroscopy. *Chemphyschem*, 2006, 7(7): 1428–1430
179. Böhme R, Richter M, Cialla D, Rösch P, Deckert V, Popp J. Towards a specific characterisation of components on a cell surface-combined TERS-investigations of lipids and human cells. *Journal of Raman Spectroscopy: JRS*, 2009, 40(10): 1452–1457
180. Bailo E, Deckert V. Tip-enhanced Raman spectroscopy of single RNA strands: towards a novel direct-sequencing method. *Angeordnete Chemie (International ed. in English)*, 2008, 47(9): 1658–1661
181. Deckert-Gaudig T, Bailo E, Deckert V. Tip-enhanced Raman scattering (TERS) of oxidised glutathione on an ultraflat gold nanoplate. *Physical chemistry chemical physics: PCCP*, 2009, 11(34): 7360–7362
182. Yeo B S, Amstad E, Schmid T, Stadler J, Zenobi R. Nanoscale probing of a polymer-blend thin film with tip-enhanced Raman spectroscopy. *Small*, 2009, 5(8): 952–960
183. van Schrojenstein Lantman E M, Deckert-Gaudig T, Mank A J G, Deckert V, Weckhuysen B M. Catalytic processes monitored at the nanoscale with tip-enhanced Raman spectroscopy. *Nature Nanotechnology*, 2012, 7(9): 583–586
184. Wang X, Zhang D, Braun K, Egelhaaf H J, Brabec C J, Meixner A J. High-resolution spectroscopic mapping of the chemical contrast from nanometer domains in P₃HT: PCBM organic blend films for solar-cell applications. *Advanced Functional Materials*, 2010, 20(3): 492–499
185. Lee N, Hartschuh R D, Mehtani D, Kisliuk A, Maguire J F, Green M, Foster M D, Sokolov A P. High contrast scanning nano-Raman spectroscopy of silicon. *Journal of Raman Spectroscopy: JRS*, 2007, 38(6): 789–796
186. Hayazawa N, Yano T, Watanabe H, Inouye Y, Kawata S. Detection of an individual single-wall carbon nanotube by tip-enhanced near-field Raman spectroscopy. *Chemical Physics Letters*, 2003, 376(1–2): 174–180
187. Hoffmann G G, de With G, Loos J. Micro-Raman and tip-enhanced Raman spectroscopy of carbon allotropes. *Macromolecular Symposia*, 2008, 265(1): 1–11
188. Neacsu C C, Dreyer J, Behr N, Raschke M B. Scanning-probe Raman spectroscopy with single-molecule sensitivity. *Physical Review B: Condensed Matter and Materials Physics*, 2007, 75(23): 193406
189. Zhang R, Zhang Y, Dong Z C, Jiang S, Zhang C, Chen L G, Zhang L, Liao Y, Aizpurua J, Luo Y, Yang J L, Hou J G. Chemical mapping of a single molecule by plasmon-enhanced Raman scattering. *Nature*, 2013, 498(7452): 82–86
190. Yeo B S, Zhang W, Vannier C, Zenobi R. Enhancement of Raman signals with silver-coated tips. *Applied Spectroscopy*, 2006, 60(10): 1142–1147
191. Cui X, Zhang W, Yeo B S, Zenobi R, Hafner C, Erni D. Tuning the resonance frequency of Ag-coated dielectric tips. *Optics Express*, 2007, 15(13): 8309–8316
192. Ichimura T, Watanabe H, Morita Y, Verma P, Kawata S, Inouye Y. Temporal fluctuation of tip-enhanced Raman spectra of adenine molecules temporal fluctuation of tip-enhanced Raman spectra of adenine molecules. *Journal of Physical Chemistry C*, 2007, 111(26): 9460–9464
193. Hayazawa N, Yano T A, Kawata S. Highly reproducible tip-enhanced Raman scattering using an oxidized and metallized silicon cantilever tip as a tool for everyone. *Journal of Raman Spectroscopy: JRS*, 2012, 43(9): 1177–1182
194. Jahng J, Tork Ladani F, Khan R M, Potma E O. Photo-induced force for spectroscopic imaging at the nanoscale. *Proceedings of the Society for Photo-Instrumentation Engineers*, 2016, 9764: 97641J
195. Nowak D, Morrison W, Wickramasinghe H K, Jahng J, Potma E, Wan L, Ruiz R, Albrecht T R, Schmidt K, Frommer J, Sanders D P, Park S. Nanoscale chemical imaging by photoinduced force microscopy. *Science Advances*, 2016, 2(3): e1501571
196. Rajapaksa I, Uenal K, Wickramasinghe H K. Image force microscopy of molecular resonance: a microscope principle. *Applied Physics Letters*, 2010, 97(7): 073121
197. Rajapaksa I, Kumar Wickramasinghe H. Raman spectroscopy and microscopy based on mechanical force detection. *Applied Physics Letters*, 2011, 99(16): 161103
198. Huang F, Tamma V A, Mardy Z, Burdett J, Wickramasinghe H K. Imaging nanoscale electromagnetic near-field distributions using optical forces. *Scientific Reports*, 2015, 5(1): 10610
199. Jahng J, Fishman D A, Park S, Nowak D B, Morrison W A, Wickramasinghe H K, Potma E O. Linear and nonlinear optical spectroscopy at the nanoscale with photoinduced force microscopy. *Accounts of Chemical Research*, 2015, 48(10): 2671–2679
200. Jahng J, Brocious J, Fishman D A, Yampolsky S, Nowak D, Huang F, Apkarian V A, Wickramasinghe H K, Potma E O. Ultrafast pump-probe force microscopy with nanoscale resolution. *Applied Physics Letters*, 2015, 106(8): 083113
201. Murdick R A, Morrison W, Nowak D, Albrecht T R, Jahng J, Park S. Photoinduced force microscopy: a technique for hyperspectral nanochemical mapping. *Japanese Journal of Applied Physics*, 2017, 56(8): 08LA04
202. Jahng J, Brocious J, Fishman D A, Huang F, Li X, Tamma V A, Wickramasinghe H K, Potma E O. Gradient and scattering forces

- in photoinduced force microscopy. *Physical Review B: Condensed Matter and Materials Physics*, 2014, 90(15): 155417
203. Jahng J, Ladani F T, Khan R M, Li X, Lee E S, Potma E O. Visualizing surface plasmon polaritons by their gradient force. *Optics Letters*, 2015, 40(21): 5058–5061
204. Tumkur T U, Yang X, Cerjan B, Halas N J, Nordlander P, Thomann I. Photoinduced force mapping of plasmonic nanostructures. *Nano Letters*, 2016, 16(12): 7942–7949
205. Tamma V A, Huang F, Nowak D, Kumar Wickramasinghe H. Stimulated Raman spectroscopy and nanoscopy of molecules using near field photon induced forces without resonant electronic enhancement gain. *Applied Physics Letters*, 2016, 108(23): 233107
206. Ambrosio A, Devlin R C, Capasso F, Wilson W L. Observation of nanoscale refractive index contrast via photoinduced force microscopy. *ACS Photonics*, 2017, 4(4): 846–851